On-Ground RFI Mitigation for Spaceborne Multichannel SAR Systems Using Auxiliary Beams

Tobias Bollian, *Member, IEEE*, Marwan Younis, *Fellow, IEEE*, Gerhard Krieger, *Fellow, IEEE*, and Alberto Moreira, *Fellow, IEEE*

***Abstract*— Radio frequency interference (RFI) is becoming a major concern for future synthetic aperture radar (SAR) missions due to the increased user demand for frequency occupation in a number of applications. Each occurrence of interference introduces artifacts in the radar imagery, biasing the measurements and leading to erroneous results. In addition to conventional techniques, the use of multichannel SAR for RFI mitigation has been proposed, because its digital beamforming (DBF) capability allows for a spatial filtering of the received signals. Thereby, it becomes possible to remove RFI that arrives from a different direction than the SAR signal. Past publications on the topic presented highly flexible spatial filtering techniques. Those methods require either additional on-board processing or a substantial increase in the downlink capacity. This article shows that by slightly reducing the flexibility of the spatial filtering, DBF can be utilized for RFI mitigation without either drawbacks: the processing is performed on-ground after downlinking the data and the data volume remains manageable. This is achieved with auxiliary beams. Their concept and limitations are discussed in detail in this article and are supported with simulated RFI mitigation results. Furthermore, it is shown that the information collected with an auxiliary beam can also be used to filter the RFI signal when it is spatially nonorthogonal to the SAR signal.**

***Index Terms*— Digital beamforming (DBF), radio frequency interference (RFI), synthetic aperture radar (SAR).**

I. Introduction

RADIO frequency interference (RFI) refers to signals transmitted by electromagnetic sources external to a synthetic aperture radar (SAR) [1], [2] system. These disturbance signals overlap with the desired radar echoes at the receiving antenna; an unavoidable side effect caused by the finite nature of the frequency spectrum [3]. Consequently, the growing demand for wireless services has increased mutual interference over time: the European Space Agency (ESA) reported only ten RFI cases [4] within the 20-year operation of European Remote Sensing (ERS) -1/2 (1991–2011), while the Sentinel-1 mission, launched in 2014, is constantly affected by interference in urban areas [5]. In addition, a study by MacDonald Dettwiler Associates found an average backscatter increase of 3 dB from 1996 to 2012 over Ottawa, Canada, likely caused by RFI [4]. Many other SAR systems have reported interferences across the P-, L-, and C-bands [6]–[11]. This trend is expected to continue [12], [13], because frequency bands assigned to spaceborne SAR are shared with other services [14].

Once RFI contaminates SAR data, it biases the measured amplitudes, corrupts polarimetric signatures, and decorrelates interferometric images [6], [7]. This effect is clearly visible in the cases of strong RFI, in which case contaminated data can be discarded at the expense of coverage. However, weak RFI is hard to spot and, if undetected, impacts the integrity of the derived science products. Unfortunately, a precise prediction of RFI occurrence and characteristics is impossible, as the properties vary locally and temporally. This variation can take place within minutes or over a span of years. The interference environment can change substantially between the conceptual design of an SAR and its operational phase. Effective RFI mitigation is therefore critical for the successful operation of an SAR mission.

Conventional RFI mitigation techniques can be grouped into three categories [15]: notching methods [7], [16]–[19], subtraction methods [20], [21], and filter methods [22]–[25]. The notching methods flag RFI-corrupted samples and remove them. For example, pulsed interference is easily notched in the time domain, whereas narrowband RFI is eliminated in the frequency domain. This is accomplished at a low computational cost; however, the SAR signal in these corrupted samples is lost as well. Consequences include gaps in the image, degraded resolution, and increased sidelobes [16]. The subtraction methods model the RFI based on *a priori* information [15], [20], [21]. A coherent subtraction of the estimated interference corrects the data without distorting the SAR signal, though the quality of the results depends on the accuracy of the estimation model. This is problematic, as attaining accurate *a priori* information is challenging due to the large spatial and temporal variability of RFI, as mentioned earlier. The final category consists of filtering methods and is divided into statistical filters and spatial filters. Statistical filters can predict the uncorrupted image if SAR and RFI signal possess different properties. Examples include the least mean square (LMS) filter applied in [22] and [23], independent component analysis [26], and blind source separation [27]. Nevertheless, the performance of these statistical filters relies on a careful selection of algorithm parameters, which depend on the SAR-to-RFI level and the RFI properties. This makes them unsuitable for SAR missions that acquire large amounts of data each day.

The method presented in this article is a spatial filter and thus performs independent of the interferer statistics and the

Manuscript received June 9, 2021; revised September 10, 2021 and December 3, 2021; accepted January 16, 2022. Date of publication January 26, 2022; date of current version March 17, 2022. *(Corresponding author: Tobias Bollian.)*

The authors are with the Microwaves and Radar Institute, German Aerospace Center (DLR), 82234 Wessling, Germany (e-mail: tobias.bollian@dlr.de).

Digital Object Identifier 10.1109/TGRS.2022.3146789

SAR-to-RFI ratio. A well-known spatial filter is the sidelobe canceller (SLC) [28]–[30], which uses an additional antenna to record an interferer in the SAR antenna's sidelobe with a high gain. The information that is gathered with the additional antenna is coherently subtracted from the data and the RFI is thus spatially filtered. This works well if the RFI direction is known. The SLC has been investigated in the context of SAR in [31], [32], and [33]. For example, in [34], a phased array is used to adapt the SLC direction of every few pulses. However, this approach suffers from the following disadvantages.

1) An additional antenna is needed for every interferer (note that even one additional antenna significantly increases the cost and complexity of an SAR system).
2) Only out-of-swath interference can be filtered. As SAR systems pursue larger swaths, this severely limits the filtering capabilities of the SLC.
3) The estimation of the interferer direction requires skipping SAR pulses. This is problematic for the advanced staggered SAR mode. In addition, such an Angle of Arrival (AoA) estimation cannot adjust to quickly changing interferer environments.

In a previous article [35], we had proposed spatial filtering with digital beamforming (DBF) [36] and overcame the drawbacks of the SLC. New, advanced SAR systems, such as DLR's Tandem-L [37], NASA-ISRO Synthetic Aperture Radar (NISAR) [38], Advanced Land Observing Satellite-4 (ALOS-4) [39], Radar Observing System for Europe-L-Band (ROSE-L) [40], and Sentinel-1NG [41], incorporate a multichannel architecture that enables DBF [42]. One advantage of DBF is the forming of the antenna pattern in postprocessing [43]. This comes at the cost of an increased system complexity; however, this complexity is already available in future systems for achieving a high azimuth resolution and a large swath width at the same time [e.g., Scan-on-Receive (SCORE) [44]], and the same technology can be used for RFI mitigation. With DBF-based spatial filtering, there is the following.

1) No need for additional antennas.
2) In-swath interference can partially be filtered.
3) The antenna pattern can be adopted range-dependently (e.g., an optimized antenna pattern for each pixel).
4) The AoA of the RFI can be estimated from the data in postprocessing.

At the same time, the high flexibility of multichannel systems has the disadvantage of an increased data volume, as the RFI removal cannot be performed by means of an on-board processing with today's field programmable gate array (FPGA) technology. Employing DBF-based spatial filtering thus puts high demands on the downlink or the on-board processing capabilities of future SAR systems. Therefore, this work proposes a novel method based on auxiliary beams, which allows for an on-ground RFI mitigation by significantly reducing the downlinked data volume. Note that this article assumes that all RFI sources are point sources and thus excludes the reflections of spaceborne RFI from the Earth's surface.

This article is organized as follows. Sections II-A and II-B introduce the concept of DBF-based auxiliary beams and explain how they can help with the RFI mitigation. The downlinked RFI information is then used in Section II-C to correct the SAR data. This is followed by a theoretical examination of the amount of RFI information lost due to spatial overlap between in-swath interferers and SAR signal (Section III). Next, Section IV presents a novel method for modeling this lost RFI information based on the information collected with an auxiliary beam. The theoretical part of this article is then closed with a discussion on the maximum number of interferers that can be removed (Section V) and a variety of different auxiliary beam implementations are presented in Section VI. Afterward, a DBF system is simulated (Section VII) and RFI mitigation performance results are presented in Sections VII-C and VII-D. This article ends with a conclusion in Section VIII.

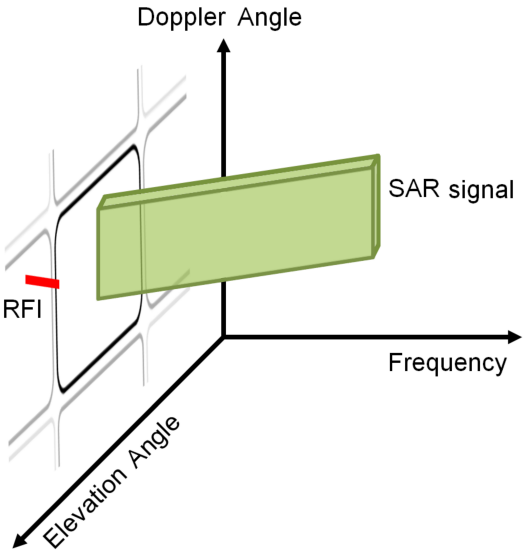

Fig. 1. Instantaneous SAR signal (green) and RFI signal (red) arrive at the antenna at the same time. The plot shows a fixed point in time and the different frequency components of the SAR signal arrive from slightly different elevation angles due to the pulse extent on the ground [45]. Although the signals overlap in frequency, multichannel systems can distinguish between both signals, if they arrive from different Doppler or elevation angles.

II. Spatial Filtering Using Auxiliary Beams

A. General Concept

The filtering space (the signal representation in which RFI orthogonal to the signal can be removed) in a conventional SAR system is limited to the frequency domain. Here, it is only possible to filter RFI from the receive window, if the SAR bandwidth is oversampled and the recorded RFI frequency falls outside of the signal bandwidth.

Multichannel SAR systems open up additional filtering space due to their ability to separate signals arriving from different angular directions as illustrated in Fig. 1 for a single echo window. The figure shows a green SAR signal and a red RFI signal, which overlap in frequency. Note that the SAR signal is distributed and spans multiple Doppler angles, while the Doppler modulation of the RFI point source is negligible within a single echo window. While a conventional SAR system cannot distinguish between the signals, a multichannel SAR system can filter out certain spatial directions (corresponding to the elevation and Doppler angles) other than the SAR signal direction.

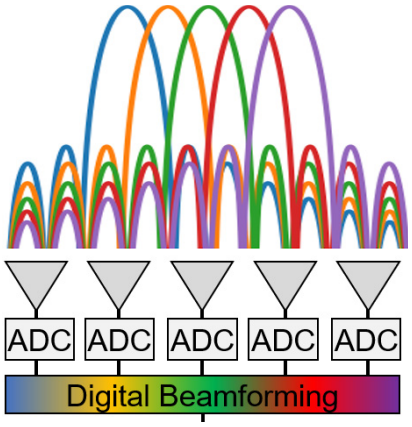

Fig. 2. DBF system records the data from each antenna subelement individually. The weighting and summation of the data streams control the antenna pattern shape after the data acquisition.

Unlike conventional systems, this allows for an RFI mitigation independent of interferer characteristics. Furthermore, the main drivers for the spatial filter performance are not scene-varying algorithm parameters but fixed system parameters: primarily, the antenna area and the number of channels.

In the multichannel SAR, the antenna is subdivided into elements (each element may, for example, correspond to a subarray) such that the data stream from each element is digitized by its own analog-to-digital converter (ADC), producing N data streams $x_n(\tau)$ with $n = 1, \ldots, N$ (Fig. 2). The multiplication of the data streams by the beamforming weights w_n and the subsequent summation is called DBF

$$s_{\mathrm{DBF}}(\tau) = \sum_{n=1}^{N} w_n x_n(\tau). \tag{1}$$

Depending on the chosen beamforming weights, the main beam of the antenna is steered into different directions. However, unlike a phased array, it is possible to synthesize multiple beams simultaneously. Specifically, the antenna pattern nulls can be carefully placed *a posteriori* after data acquisition. This makes DBF a powerful tool.

While a conventional SAR system requires a sufficiently small receive antenna to cover the entire swath with a wide beam [yellow box in Fig. 3(a)], the DBF-based SCORE [44], [46] employs a tall antenna with a moving narrow beam [blue polygon in Fig. 3(a)]. This narrow beam steers toward the expected radar return [green curve in Fig. 3(a)], thus achieving a higher signal-to-noise ratio (SNR). This AoA change of the radar return is inherent to the side-looking imaging geometry and can also be used for an improved spatial RFI filtering. From Fig. 3(a), it is evident that an in-swath interferer (red line) is only within the SCORE beam for a fraction of the receive window echo time. This is in direct contrast to a conventional SAR system that observes the same RFI through the main lobe (yellow box) during the entire receive window and thus cannot spatially filter the interferer.

The DBF-based RFI mitigation we proposed in [35] makes use of this predetermined change of the SAR signal direction over time. However, this requires either adaptive DBF processing on-board or downlinking of all channels to the ground.

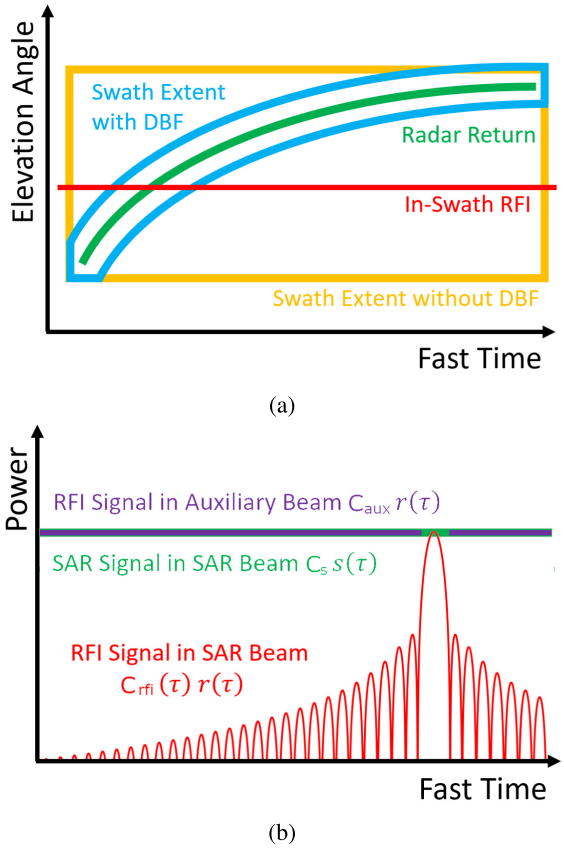

Fig. 3. (a) SAR signal direction within the receive window (green curve). The yellow box represents the necessary beamwidth of a conventional SAR and the blue polygon represents the narrower beam with DBF. A partial spatial filtering of the in-swath RFI (red line) is possible with the narrower beam. (b) Fixed SAR radiation pattern C_s (green curve) in the moving SCORE beam, modulated RFI radiation pattern $C_{\mathrm{rfi}}(\tau)$ (red curve) in SCORE beam, and fixed RFI radiation pattern C_{aux} in auxiliary beam (purple curve).

Both the options are not feasible with the next generation of SAR systems due to the too large data volume that would need to be processed or transmitted. Therefore, this article proposes a new method that uses DBF to form multiple antenna beams simultaneously. This is possible by applying different weights to the digitized data stream of each antenna element after the data are recorded on-board. Hence, while the SCORE beam moves along the ground and captures the SAR signal, a DBF system can point additional beams—called auxiliary beams—toward RFI sources. As will be detailed in the following sections, these auxiliary beams can be employed at a low computational cost, because their digital weights can be computed *a priori* for the mitigation of known RFI directions or the cancellation of interference within the first SCORE sidelobes. An on-the-fly estimation of the interferer directions also allows for the recording of unknown RFI sources, whereas unknown but very strong interferers can be recorded without the knowledge of their position. The RFI information measured with auxiliary beams is then transmitted to the ground, where it can be used for RFI mitigation in post-processing. While the downlinked data volume depends on the number of interferers and their bandwidth, it is significantly reduced compared with downlinking all digital channels.

B. Signal Model and Operation

The measured SCORE beam signal is given by

$$s_{\mathrm{DBF}}(\tau) = GC_{\mathrm{s}}s(\tau) + GC_{\mathrm{rfi}}(\tau)r(\tau) \tag{2}$$

where G is the antenna gain, and the desired radar return $s(\tau)$ is weighted by the SCORE radiation pattern C_{s} and the unwanted RFI signal $r(\tau)$ is weighted by $C_{\mathrm{rfi}}(\tau)$. Note that C_{s} is more or less constant and close to one, because the SCORE beam changes the direction over time and always collects the radar return with the peak gain. On the other hand, the RFI radiation pattern varies because of the aforementioned sweeping of the SCORE beam. The recorded signal power after beamforming is illustrated in Fig. 3(b), assuming $s(\tau) = r(\tau) = 1$ before beamforming.

Simultaneous to the SCORE beam, a so-called auxiliary beam is formed that points at the interferer and notches the SAR signal (a notching of the SAR signal is only possible with DBF, because the notch position changes with fast time τ)

$$s_{\mathrm{aux}}(\tau) = GC_{\mathrm{aux}}r(\tau) + GM_{\mathrm{z}}(\tau)s(\tau). \tag{3}$$

The interferer radiation pattern C_{aux} in the auxiliary beam is constant, because the auxiliary beam points to a fixed direction. On the other hand, the SAR signal is modulated with a small function $M_{\mathrm{z}}(\tau)$, because the notch toward the SAR signal is only ideal for the center frequency of the radar pulse, and the suppression degrades at the frequency edges of the spectrum. (The edges of the instantaneous SAR signal will arrive from slightly different directions due to the pulse extent. This is discussed in detail in [45].) However, the amount of this degradation can be reduced with a dispersive beamforming, and a residual modulation is acceptable as long as $|M_{\mathrm{z}}(\tau) < C_{\mathrm{aux}}|$. This condition is fulfilled everywhere except inside an estimation gap, which arises for the period when the RFI and SCORE signals overlap spatially [interruption of purple line in Fig. 3(b), corresponding to the red line of Fig. 3(a) entering the blue polygon].

The RFI is removed from the data (except for within the estimation gap) by scaling and coherently subtracting the auxiliary beam as shown in Fig. 4. This complex scaling coefficient $k(\tau)$ is obtained by requiring that the scaling equalizes the RFI components of (2) and (3) according to

$$k(\tau)GC_{\mathrm{aux}}r(\tau) = GC_{\mathrm{rfi}}(\tau)r(\tau) \tag{4}$$

and yields

$$k(\tau) = \frac{C_{\mathrm{rfi}}(\tau)}{C_{\mathrm{aux}}}. \tag{5}$$

The corrected signal $s_{\mathrm{c}}(\tau)$ is thus obtained by scaling (3) with (5) and subtracting the result from (2)

$$s_{\mathrm{c}}(\tau) = Gs(\tau)\left[C_{\mathrm{s}} - \frac{M_{\mathrm{z}}(\tau)C_{\mathrm{rfi}}(\tau)}{C_{\mathrm{aux}}}\right]. \tag{6}$$

The introduced error term when $M_{\mathrm{z}}(\tau) \neq 0$ remains negligible as long as the auxiliary beam and the SCORE beam point in different directions, because, in this case, $C_{\mathrm{rfi}}(\tau)/C_{\mathrm{aux}}$ is sufficiently small. An overlap of both the beams occurs only in the estimation gap, where the RFI cannot be spatially filtered (a novel approach for correcting RFI in the estimation gap is discussed in Section IV).

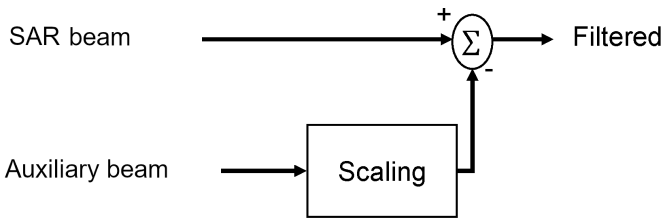

Fig. 4. Interferer information collected with the auxiliary beam is coherently subtracted from the SAR data after applying an appropriate scaling.

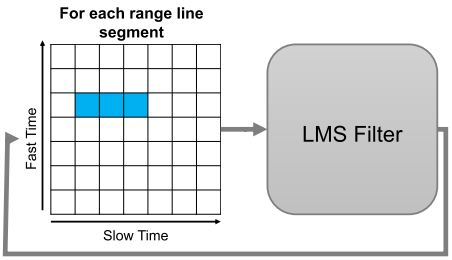

Fig. 5. LMS filter estimates the complex scaling coefficient $k(\tau, t)$ on small segments along slow time.

The RFI measured with the auxiliary beam can be downlinked to the ground, where $k(\tau)$ is derived from the data (see Section II-C) for an optimal RFI mitigation.

C. Estimation of the Scaling Coefficient

Once the SAR data and the auxiliary beam information are downlinked, the RFI mitigation is applied on ground. This basically consists of an estimation of the complex scaling coefficient $k(\tau)$ from (5), for example, by means of an LMS optimization.

The recorded SAR signal $s_{\mathrm{DBF}}(\tau, t)$ is represented by a 2-D matrix with the dimensions τ (fast time) and t (slow time). Identically, the recorded RFI information $s_{\mathrm{aux}}(\tau, t)$ corresponds to a 2-D matrix. Hence, there exists an optimum, complex scaling coefficient $k(\tau, t)$ for each point in these matrices. $k(\tau, t)$ can be estimated by realizing that the SCORE beam performs a repetitive scanning, which repeats for each receive window (azimuth position). The scaling is therefore assumed constant in slow time

$$k(\tau, t_i) \approx k\left(\tau, t_j\right) \tag{7}$$

for every i and j. This assumption is valid for a planar antenna. For a reflector antenna, an estimation of the relative azimuth pattern could be incorporated [47].

This allows to apply the estimation as an LMS filter with windows in the slow-time dimension (azimuth), as shown in Fig. 5, on small segments of the matrices. Another option is to apply the filter with a moving window. The optimum complex scaling coefficient of each window is estimated with the well-known LMS solution [48], [49], which minimizes the power in the filtered data

$$k(\tau) = \left[s_{\mathrm{aux}}(\tau, t)s_{\mathrm{aux}}(\tau, t)^H\right]^{-1} s_{\mathrm{aux}}(\tau, t)s_{\mathrm{DBF}}(\tau, t)^H \tag{8}$$

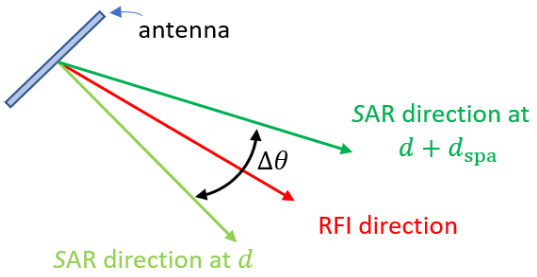

Fig. 6. Antenna cannot differentiate between RFI and SAR signals in the angular area $\Delta\theta$. The time duration d_{spa} of this overlap is determined by how fast the SAR signal sweeps through this angular area.

in which case $s_{aux}(\tau,t)s_{aux}(\tau,t)^H$ is a scalar and inverse exists. Note that τ is the parameter and the resulting vectors are column vectors.

This can be efficiently computed on the entire data via

$$k = \left[\frac{1}{\mathrm{diag}\left(s_{aux}s_{aux}^H\right)} \otimes \mathrm{diag}\left(s_{aux}s_{DBF}^H\right)\right] \tag{9}$$

where $\otimes$ represents an elementwise multiplication.

III. Estimation Gap for In-Swath RFI

As mentioned in Section II, an estimation gap remains in the auxiliary beam information if the RFI is emitted from within the swath. The size of this gap can be controlled in the system design, and the individual contributions to this gap are discussed in this section. The gap arises during the spatial overlap of the RFI and the SCORE signals and its slant-range extent d_{gap} is given by

$$d_{gap} = d_{spa} + d_{top} + d_{att} + d_{sub} \tag{10}$$

where the largest component, d_{spa}, is due to the antenna's ability to spatially separate two signals. d_{spa} can be controlled during the system design as discussed in Section III-A. d_{top} is introduced by uncertainties in the imaged terrain height (Section III-B, typically below 1.5 km); d_{att} is a result of attitude uncertainties (Section III-C); and d_{sub} is due to the pulse duration of the transmitted radar chirp, which is in the order of 10–30 km if no dispersive processing is applied (Section III-D).

A. Impact of the Spatial Resolution

The main driver of the estimation gap length is d_{spa} (Fig. 6) during which the antenna cannot separate between RFI and SAR signals. d_{spa} is determined by two criteria.

1) The antenna's ability to spatially distinguish signals separated by the angular interval $\Delta\theta$.
2) How fast the SAR signal sweeps across this angular area $\Delta\theta$.

Consequently, the estimation gap component due to the spatial resolution is

$$d_{spa} = \frac{c_0\Delta\tau}{2\Delta\vartheta_l}\Delta\theta \tag{11}$$

with the inverse of the SAR signal sweep velocity $\Delta\tau/\Delta\vartheta_l$. This section first discusses $\Delta\theta$ and then derives d_{spa} using the SAR signal sweep velocity.

In a conventional SAR, $\Delta\theta$ is often approximated by the 3-dB-beamwidth [50]

$$\Delta\theta_{conv} = \frac{\lambda}{h_a}\gamma \tag{12}$$

where λ is the wavelength, h_a is the antenna height, and γ equals 1.0 for planar antennas and 1.4–1.5 for reflector antennas. However, a DBF system allows for the innovative notching of the instantaneous SAR signal direction inside the auxiliary beam. This notch aids the separation at the cost of an interferer gain drop [C_{aux} drops in (3)], as the SCORE beam sweeps over the interferer position, which is shown in Fig. 7(a) (purple curve). This means that the spatial resolution improves with the SNR in the auxiliary beam SNR_{aux}. Therefore, it is possible to improve the spatial resolution if either.

1) The measured RFI is strong and remains above the noise floor even if C_{aux} drops.
2) The measured RFI is bandpass-filtered to improve the SNR. This allows measuring weak RFI despite a reduced C_{aux}.

Note that the second option requires the RFI bandwidth to be smaller than the SAR bandwidth.

We therefore define the angular resolution of the DBF system as

$$\Delta\theta_{DBF} = \zeta\,\Delta\theta_{conv} \tag{13}$$

where $\zeta < 1$ is a resolution factor that accounts for the benefit of the innovative notching of the SAR signal inside the auxiliary beam. Note that improving SNR_{aux} allows for a smaller ζ.

The influence of the angular resolution on the estimation gap length is then calculated by inserting $\Delta\theta_{DBF}$ into (11). The sweeping velocity is computed via [45]

$$\frac{\Delta\vartheta_l}{\Delta\tau} = \frac{c_0}{2r_O\left(\frac{r_O\cos\theta_l}{\sqrt{r_E^2 - r_O^2\sin^2\theta_l}} - 1\right)\sin\theta_l}. \tag{14}$$

Hence, the estimation gap length due to the antenna is

$$d_{spa} = r_O\zeta\,\Delta\theta_{conv}\left(\frac{r_O\cos\theta_l}{\sqrt{r_E^2 - r_O^2\sin^2\theta_l}} - 1\right)\sin\theta_l. \tag{15}$$

Fig. 7(b) shows d_{spat} versus h_a/λ for: 1) a system with $H = 745$ km at $\theta_l = 35.13°$ (solid lines); 2) a system with $H = 745$ km at $\theta_l = 23.98°$ (dashed lines); and 3) a system with $H = 545$ km at $\theta_l = 35.13°$ (dotted lines). It is evident that d_{spa} is largest in far range and increases with altitude because of the slower SCORE beam velocity.

B. Impact of Topography

Measuring the RFI requires a sufficient suppression of the SAR signal in the auxiliary beam. This suppression is inherently achieved if the RFI and SAR separation is larger than the spatial resolution discussed in Section III-A. However,

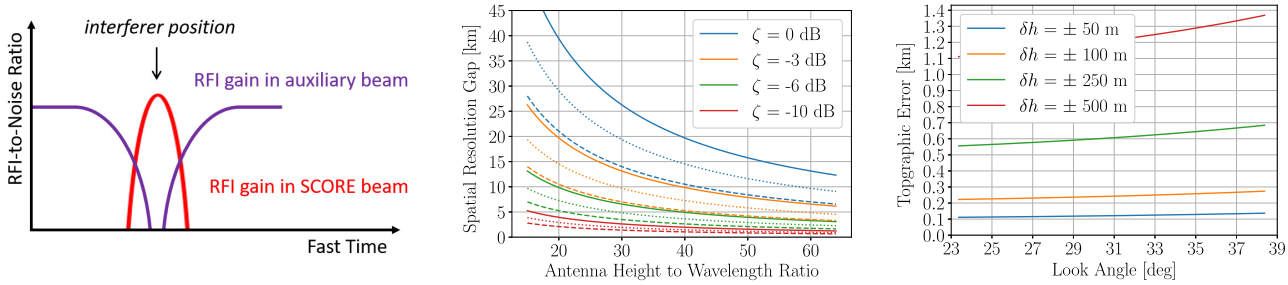

(a) (b) (c)

Fig. 7. (a) RFI gain in the auxiliary beam (purple) drops while the RFI signal and the SAR signal overlap spatially. (b) Estimation gap increases due to the antenna's angular resolution for $H = 745$ km at $\theta_l = 35.13°$ (solid lines), $H = 745$ km at $\theta_l = 23.98°$ (dashed lines), and $H = 545$ km at $\theta_l = 35.13°$ (dotted lines). (c) Estimation gap increases due to topographic uncertainty δh. ζ refers to the resolution factor of a DBF system defined in (13).

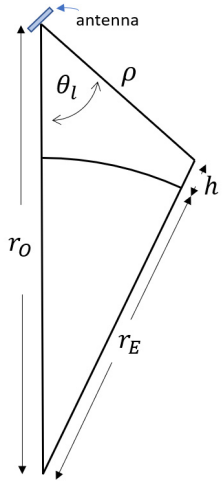

Fig. 8. Orbit and slant-range geometry for a spherical Earth.

an uncertainty in topography shifts the resulting estimation gap, which is crucial, because applying the RFI correction inside the estimation gap corrupts the SAR signal. The effective estimation gap is thus increased by the uncertainty in the topography.

The relationship between slant range ρ and look angle θ_l can be derived from Fig. 8 according to

$$\rho = r_O \cos\theta_l - \sqrt{(r_E + h)^2 - r_O^2 \sin^2\theta_l} \tag{16}$$

with the Earth radius r_E, the topographic height h, the satellite altitude H, and $r_O = r_E + H$. From (16), it is evident that the slant range at the look angle θ_l, and thus the two-way travel time $2\rho/c_0$, depends on the topography. Introducing an uncertainty in the terrain knowledge, δh results in a slant-range error $\delta\rho$. Computing the slant range with the modified height using (16) and subtracting the nominal height yield the range delay error

$$d_{top} = 2\left|\delta\rho\right| = 2\left|\sqrt{(r_E + h + \delta h)^2 - r_O^2 \sin^2\theta_l} - \sqrt{(r_E + h)^2 - r_O^2 \sin^2\theta_l}\right|.$$

The notch inside the auxiliary beam (toward the radar return) can be widened to accommodate this uncertainty, effectively increasing the estimation gap.

d_{top} is plotted in Fig. 7(c) for a system with $H = 745$ km and $h = 0$ km. For topographic uncertainties of $\delta h \pm 100$ m, d_{top} is at least one order of magnitude smaller than d_{spa}.

C. Impact of Satellite Attitude

Another contribution to the estimation gap is uncertainties in the satellite pointing due to attitude errors. Using (16) as a function of θ_l, the effect of the attitude error in elevation $\delta\theta$ can be computed as

$$d_{att} = 2|\rho(\theta_l + \delta\theta) - \rho(\theta_l)|. \tag{17}$$

For a reflector-based system like Tandem-L, $\delta\theta$ is in the order of 0.04°. A system with such an error operated at $H = 745$ km and for $h = 0$ km is affected by $d_{att} = 0.6$ km and $d_{att} = 1.3$ km at $\theta_l = 24.3°$ and $\theta_l = 38°$, respectively. For a planar-based system, $\delta\theta$ is in the order of 0.01° and the impact of d_{att} stays below 1 km.

D. Impact of the Pulse Duration

The RFI source on the ground is illuminated by the radar pulse during τ_p seconds, i.e., the radar pulse duration. During this time, the measurement of the RFI signal through the auxiliary beam is deteriorated and cannot be fully resolved by spatial filtering. The corresponding gap extent can be reduced with a subband-dependent notching of the auxiliary beam (dispersive beamforming). Consequently, RFI which is only occupying one subband is illuminated by the radar pulse for the reduced duration

$$d_{sub} = \frac{c_0 \tau_p B_{sub}}{2B_s} \tag{18}$$

with the radar bandwidth B_s and the subband bandwidth B_{sub}. For commonly used pulse durations, only few subbands are necessary to keep d_{sub} at least one order of magnitude smaller than d_{spa}.

IV. Estimation Gap Reconstruction for In-Swath RFI

This section shows that the RFI inside the estimation gap, where spatial filtering is not possible, can be removed with auxiliary beams under the right conditions. The estimation gap is filled by means of an interpolation or modeling (Fig. 9) in postprocessing on the ground: the auxiliary beams collect

Fig. 9. Information collected with the auxiliary beam (red) is used to model the signal inside the estimation gap.

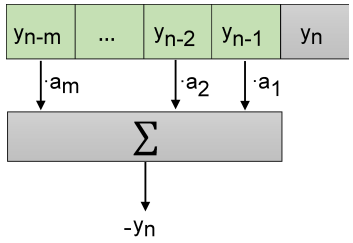

Fig. 10. Illustration of (19). Autoregressive modeling estimates the next sample y_n by weighting and summation of the previous samples (green boxes).

information about the RFI on both the sides of the estimation gap, which is used to predict the RFI signal inside the estimation gap. Hence, no *a priori* external information is needed. This article demonstrates this technique with an autoregressive model [51], [52], which is commonly applied in the restoration of digital audio signals [53], [54] and works well if the signals are stationary for the duration of the estimation gap. [Note that the estimation gap length depends on the antenna height and the RFI-to-noise ratio (RNR).]

The signal reconstruction can be achieved if a relation between the missing sample y_n and its preceding values y_{n-i} can be formed so that

$$y_n = -\sum_{i=1}^{m} a_i y_{n-i} \tag{19}$$

which weighs each known sample with a coefficient a_i and recovers y_n by means of a summation of the weighted outputs, as illustrated with the block diagram in Fig. 10. Several autoregressive methods exist that estimate the weighting coefficients by optimizing

$$\min \left(y_n + \sum_{i=1}^{m} a_i y_{n-i} \right)^2. \tag{20}$$

A stable method that minimizes the error of both the forward and backward estimations (inversion of the sample order) is the recursive Burg's method [55]–[58] and is used in this article. A detailed description of the method and its derivation, as well as the implementation, can be found in [59].

Using an autoregressive model enables the reconstruction of RFI signals that are stationary over the time duration of the estimation gap.[1] This is, for example, the case for most radio amateur signals in the P-band [60].

[1]Section III-A showed that the estimation gap is in the order of a few tens of microseconds for systems with multiple channels in elevation and defined by the imaging geometry and the system design.

If the RFI signal is not stationary over the estimation gap duration but consists of a repetitive signal (e.g., radar pulses), the gap can be filled with the recognized pattern, while more complex models could be employed for transmitters with known encoding schemes.

V. Filtering Multiple Interferers

This section explores the usage of auxiliary beams in environments with multiple interferers with regard to the technical limitations of the RFI mitigation and the implementation feasibility in current SAR systems. In general, it is possible to synthesize an arbitrary number of auxiliary beams simultaneously. Two RFI sources can be removed from the data if they are either transmitting at different frequencies or are located in nonoverlapping auxiliary beams (note that the auxiliary beam footprint in azimuth could also be reduced with azimuth beamforming). If multiple narrow auxiliary beams are used for this purpose, the AoA of each interferer needs to be known beforehand or estimated on-board. This is illustrated in Fig. 11, in which all interferers can be filtered, except for the two interferers in the bottom right footprint (due to overlap in space and frequency). The equations of such an overlapping scenario are derived in the following. Let these two problematic interferers be located at θ_1 and θ_2, with $|\theta_1 - \theta_2| < \Delta\theta_{\mathrm{DBF}}$. Consequently, the collected RFI information is a superposition of both the signals $r_1(\tau)$ and $r_2(\tau)$ according to

$$s_{\mathrm{aux}}(\tau) = r_1(\tau) G C_{\mathrm{aux}}(\theta_1) + r_2(\tau) G C_{\mathrm{aux}}(\theta_2). \tag{21}$$

Due to the small spatial distance between both the RFI signals, $C_{\mathrm{aux}}(\theta_1)$ and $C_{\mathrm{aux}}(\theta_2)$ are similar but not identical: each of the two signals has a different ideal scaling coefficient, which is in the following refered to as k_1 and k_2. However, it is not possible to scale the components of (21) individually. An on-ground estimation of the scaling coefficient will result in an effective scaling factor k_{eff}, which is then applied to (21), and the result is subtracted from the SAR data. This means that a residual RFI remains in the corrected SAR signal

$$s_{\mathrm{c}}(\tau) = G C_{\mathrm{s}} s(\tau) + r_1(\tau) G C_{\mathrm{rfi}}(\tau, \theta_1) \left[1 - \frac{k_{\mathrm{eff}}}{k_1} \right] + r_2(\tau) G C_{\mathrm{rfi}}(\tau, \theta_2) \left[1 - \frac{k_{\mathrm{eff}}}{k_2} \right].$$

The RFI mitigation only reduces the original RFI components in the image for $|[1 - (k_{\mathrm{eff}}/k_2)]| < 1$, which depends on the signal characteristics. A reliable use of auxiliary beams

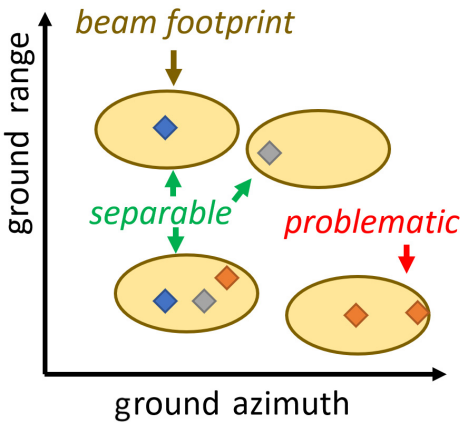

Fig. 11. Multiple interferers (diamonds) within the auxiliary beam footprint are resolved if they transmit at different frequencies (illustrated by different colors). Closely spaced interferers at the same frequency cannot be resolved and are treated as one RFI source, degrading the RFI mitigation performance.

requires accounting for the necessary spatial resolution to resolve the expected RFI environment.

In addition, it is noted that even if each interferer is illuminated with its own auxiliary beam, RFI information can leak between the beams through the sidelobes. This leakage is especially prominent for a large number of interferers and a large range of RFI powers. Nevertheless, this effect can be reduced with additional notches at the expense of beamforming complexity.

Another important factor is that increasing the number of auxiliary beams also effects the data rate and transmitted data volume. The data volume reduction F of the auxiliary beam method compared with the transmission of all digital channels to the ground is

$$F = \frac{m B_{\text{rfi}}}{(N - S) B_{\text{s}}} \tag{22}$$

where m is the number of interfering sources, B_{s} is the SAR bandwidth, B_{rfi} is the interferer bandwidth, N is the number of channels, and S is the number of SCORE beams transmitted to the ground. Equation 22 is valid, because it suffices to set the auxiliary beam bandwidth equal to B_{rfi}. Consequently, the data volume reduction factor depends on the expected interferer environment. For example, a system with 16 channels, which is exposed to four interferers transmitting with 10% of the SAR bandwidth each, will achieve $F = 0.025$. The on-ground processing with auxiliary beams reduces the transmitted data for the RFI mitigation by a factor of 40.

Downlinking all digital channels might be favorable for F close to 1, as this allows for more processing flexibility on ground.

VI. Auxiliary Beamforming Options

This section introduces multiple options for forming auxiliary beams. Each method has different advantages in terms of computational complexity and required *a priori* knowledge of the interference environment. The presented methods can measure interference inside and outside the swath.

A. Wide Beam

The easiest auxiliary beam implementation is a wide beam as shown in red in Fig. 12(a). A simultaneous notch toward the green SCORE beam suppresses the SAR signal. This notch is moving with the SCORE beam but its weights are precomputed in the same manner, as the SCORE weights are precalculated ahead of the acquisition. No AoA estimation of the interferer direction is performed, though this comes at the cost of a reduced RFI radiation pattern C_{aux}. The reduced SNR affects the size of the estimation gap as discussed in Section III-A.

B. Narrow Beam

Another option is to form a narrow auxiliary beam toward the direction of the interferer as shown in Fig. 12(b). Note that the SCORE beam direction is notched. The beam is narrower and has a higher radiation pattern C_{aux} and thus SNR, which reduces the RFI estimation gap. However, a mispointing of the beam results in a loss of the RFI information, and therefore, it is necessary to perform an on-board AoA estimation. Another option is to only use the narrow beam for interferers with a known and fixed location.

C. Interleaved Beam

The interleaved beam has a high RFI radiation pattern and yet does not require an on-board AoA estimation. This is achieved by merging two auxiliary beams that are time-shifted copies of the SCORE beam as shown in Fig. 12(c). The first beam is preceding the SCORE beam, and the second beam is following the SCORE beam with a time delay. In other words, both the beams point at the instantaneous direction of the SCORE beam's first sidelobes while notching the direction of the instantaneous SAR signal. The combination of both the auxiliary beams allows for recording the RFI in the first SCORE sidelobes with a high-radiation pattern. This is advantageous if the RFI direction is unknown and RFI in the higher-order sidelobes is sufficiently suppressed (e.g., reflector antenna). The auxiliary beam weights can easily be computed on-ground before the acquisition. Both the beams can be combined before transmitting the information to the ground.

This article focuses on beam options for a system with multiple elevation channels. However, auxiliary beams are also applicable to systems with multiple azimuth channels or with a combination of azimuth and elevation channels. The interested reader is referred to [61].

VII. Simulation of a DBF System With Auxiliary Beams

The rest of this article presents simulation results for a DBF system with auxiliary beams in elevation. The system employs a planar antenna and the system parameters are summarized in Table I. This section summarizes the simulation chain and the error model that is common to all RFI mitigation results. The presented system performance parameters SNR, RFI-to-signal ratio (RSR), and RNR are defined as

$$\text{SNR} = \frac{\bar{P}_{\text{Signal}}}{\bar{P}_{\text{Noise}}} \tag{23}$$

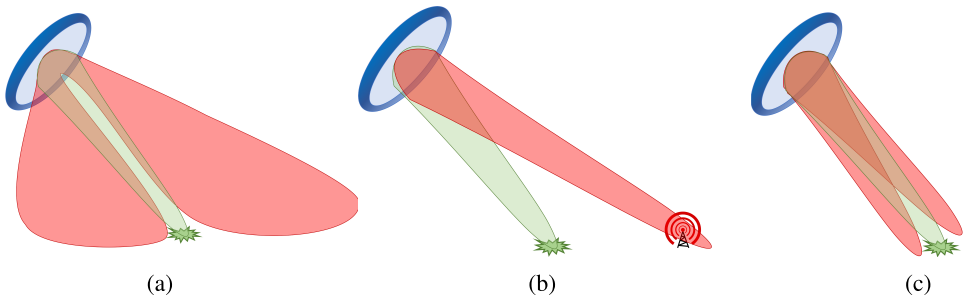

Fig. 12. Auxiliary beam implementations (red). The SAR signal is collected with the green beam and the auxiliary beam is notched toward the direction of the instantaneous radar return. (a) Wide beam with low SNR. (b) Narrow beam with high SNR. (c) Interleaved beam measures the first sidelobes and provides a high SNR.

TABLE I
SAR SYSTEM AND SIMULATION PARAMETERS

Parameter	Value
Elevation Channels	63
Channel Spacing	0.5λ
Sample Frequency	100 MHz
Center Frequency	1.2575 GHz
Chirp Bandwidth	80 MHz
Pulse Duration	20 μs
Near Range Incidence Angle	26.3°
Far Range Incidence Angle	43.9°
Array Tilt	45°
Platform Altitude	745 km
Swath Width	350 km
Backscatter Amplitude	Rayleigh distribution
Backscatter Phase	Uniform distribution (0° to 360°)
SNR	0 dB to 40 dB
PRF	2600 Hz

with the average signal power after beamforming $\bar{P}_{\text{Signal}}$ and the average noise power after beamforming $\bar{P}_{\text{Noise}}$

$$\text{RSR} = \frac{\bar{P}_{\text{RFI}}}{\bar{P}_{\text{Signal}}} \tag{24}$$

with the average RFI power after beamforming $\bar{P}_{\text{RFI}}$, and

$$\text{RNR} = \frac{\bar{P}_{\text{RFI}}}{\bar{P}_{\text{Noise}}}. \tag{25}$$

This allows relating the power in the beamformed planar system data to the power at a single reflector antenna feed.

A. RFI Simulator

This section describes the simulation chain for the performance evaluation as illustrated in Fig. 13. As an initial step, multichannel SAR raw data are simulated for the designed DBF system. The SAR data are modeled with a complex-Gaussian circular backscatter, which is a valid assumption for an extended target [50]. Hereby, each data channel is simulated in the following way.

1) A complex Gaussian noise vector is simulated and serves as a backscatter vector b.
2) A vector of look angles θ_l that corresponds to distributed points on the ground is computed.

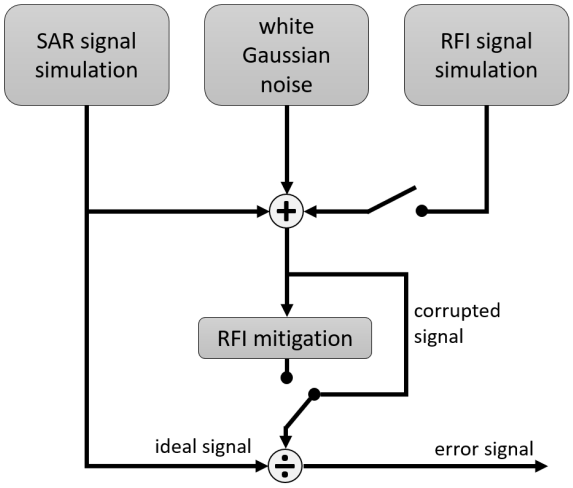

Fig. 13. Simulation chain for the performance evaluation.

3) The backscatter of channel n is computed by multiplying b by $e^{i\pi(n-1)\sin\theta_l}$, which corresponds to the phase delay due to the half-lambda spacing between channels.[2]
4) The backscatter of each channel is convoluted with the transmitted radar chirp.

Note that constant factors in the radar equation are ignored, as the simulation of the beamforming only requires to account for the relative channel differences. Next, the system applies DBF to its channels and this beamformed SAR signal serves as an ideal reference signal.

Then, error sources are simulated. These errors include system noise (modeled as additive white Gaussian noise) and,

[2]The SCORE operation that is already planned for future SAR systems requires scanning to the edges of the imaged swath without grating lobes. Concepts that are currently considered for these systems require a scanning of up to $\phi_0 = 15°$ away from the antenna boresight. Thus, the adjacent channel spacing in wavelengths (d/λ) needs to be [62] $(d/\lambda) < (1/1 + |\sin\psi_0|) = 0.79$. This also guarantees that auxiliary beams can be used for in-swath interference without the occurrence of grating lobes. Note that such a spacing still results in grating lobes when auxiliary beams are scanned outside the imaged swath. In this case, this technique remains applicable if the instantaneous SAR signal and interference are not visible in the grating lobes and main beam simultaneously. The cost for an operation without grating lobes outside of the imaged swath is a half-lambda spacing as it is simulated in this article.

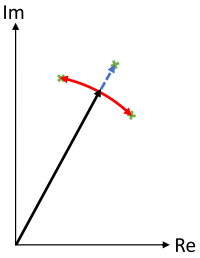

Fig. 14. Multiplicative error model: the SAR signal (black vector) is affected by a multiplicative amplitude error (blue dashed vector) and a multiplicative phase error (red).

optionally, the simulated and beamformed RFI signals (the properties of the RFI signal vary between the simulation scenarios and are discussed in the corresponding sections). A corrupted SAR signal is created by summing the error sources to the ideal reference signal. The corrupted signal is then passed to the output to analyze the degradation before filtering. The RFI signal measured by the system's auxiliary beams is simulated, and the RFI mitigation proposed in this article is applied to the data. In the end, this output signal is divided by the ideal signal so that the error model presented in Section VII-B can be used. Note that, for the purpose of generality, this article simulates a continuous-wave (CW) and binary frequency shift keying (BFSK) interferer to investigate the performance of the autoregressive modeling for RFI that is changing with various speeds w.r.t. the estimation gap duration.

B. Error Model

While RFI is an additive error, this article uses the multiplicative error model illustrated in Fig. 14. The advantage of this error model is that the multiplicative amplitude error $|\vec{e}|$ (blue dashed) directly describes the effect on the measured amplitude (black), while the multiplicative phase error $\arg(\vec{e})$ directly describes the effect on the measured phase (red). Both the errors are decoupled. Note that this is not the case for an additive error model. In the additive model, there is an interrelation between phase and amplitude errors: for example, a given phase error has a stronger impact for greater RFI amplitudes and both the errors cannot be analyzed separately. Hence, this work uses a multiplicative model

$$\vec{m}(\tau,t)=\vec{s}(\tau,t)\vec{e}(\tau,t)=[A_0+A(\tau,t)]\cdot\vec{s}(\tau,t)\cdot e^{j\Phi_0}\cdot e^{j\Phi(\tau,t)} \tag{26}$$

where A_0 and Φ_0 are constant amplitude and phase offsets and $A(\tau,t)$ and $\Phi(\tau,t)$ are time-varying errors. $A(\tau,t)$ and $\Phi(\tau,t)$ are expressed with their respective standard deviations σ_{A} and σ_{Φ}. The model is applied to unfocused raw data.

In Sections VII-C–VII-E, multiple SAR pulses are simulated, and the error model is applied to each pulse individually. A final 3-sigma error for each parameter is then computed based on the mean μ and variances σ^2 of the model parameters in the total image. This results in the 3-sigma offset errors for the amplitude and phase

$$\mu_{A_0}+3\sigma_{A_0} \tag{27}$$

and

$$\mu_{\Phi_0}+3\sigma_{\Phi_0}. \tag{28}$$

The 3-sigma standard deviation (std. dev.) errors for the amplitude and phase are

$$\mu_{A(\tau,t)}+3\sigma_{A(\tau,t)} \tag{29}$$

and

$$\mu_{\Phi(\tau,t)}+3\sigma_{\Phi(\tau,t)} \tag{30}$$

respectively.

C. Simulation Results for Out-of-Swath RFI

This section investigates the effectiveness of auxiliary beams for out-of-swath interference. An interferer is placed outside of the system's swath at $\theta_{\mathrm{I}}=-20°$. The emitted RFI signal is a continuous wave transmitting at a baseband frequency of 40 MHz. A total of 500 SAR pulses are simulated and the interferer experiences an interpulse phase offset that corresponds to a time shift of 1/pulse repetition frequency (PRF), which accounts for the fact that RFI and SAR systems are not synchronized. Because the auxiliary beam concept is a spatial filter, the system is expected to fully mitigate the RFI in this scenario.

The previously defined 3-sigma std. dev. error, in the absence of noise (which can be fully contributed to the RFI), is plotted in Fig. 15(a) before (blue) and after (orange) the auxiliary beam filter is applied. Without RFI mitigation, the error begins to move toward unacceptable values as the RSR approaches around -20 dB. The system achieves a full removal of the RFI signal with the proposed auxiliary beam method, returning the residual errors to nearly zero even for high RSR. For low RSR (smaller than -40 dB), however, a degradation of the performance is visible. The reason is that, in the absence of noise and interference, 3 results in the auxiliary beam signal

$$s_{\mathrm{aux}}(\tau)\Big|_{r(\tau)=0}=GM_{\mathrm{z}}(\tau)s(\tau). \tag{31}$$

Because $M_{\mathrm{z}}(\tau)$ attenuates and modulates the SAR signal (as the notch is only ideal for the center frequency of the SAR return), a small residual SAR signal remains, which is correlated with the SAR signal in the SCORE beam. The LMS filter tries to remove the correlated component and therefore degrades the signal. As shown in Fig. 15, this effect vanishes in the presence of noise (low SNR), but it could also be avoided with a threshold for the scaling coefficient k.

Next, system noise (additive white Gaussian noise) is added to the SAR and RFI data. All four error parameters from Section VII-B are plotted in Fig. 15(b) through Fig. 15(f). Note that the 3-sigma error increase refers to the error increase compared with the error introduced by noise only. When the RFI is above the noise floor (RNR $>$ 0 dB), and thus detectable, the LMS output error remains at zero

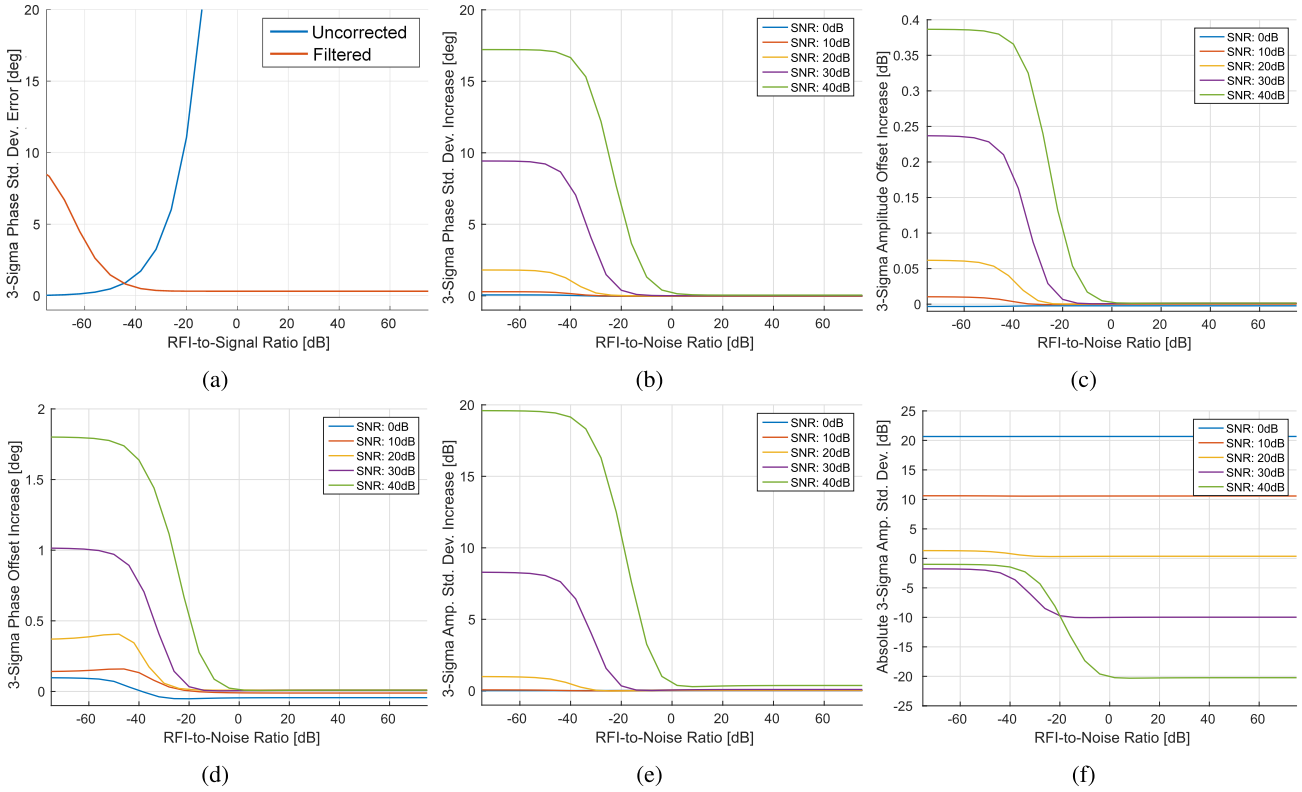

Fig. 15. 3-sigma error versus RNR in the presence of a CW interferer (40-MHz baseband, $\theta_I = -20°$) that is located out of swath. The SNR is in reference to the SAR signal. (a) Phase standard deviation in the absence of noise. (b) Phase standard deviation increase compared with noise only. (c) Amplitude offset increase compared with noise only. (d) Phase offset increase compared with noise only. (e) Amplitude standard deviation increase compared with noise only. (f) Absolute amplitude standard deviation error.

(no standard deviation increase above the normal noise floor) for all parameters regardless of SNR. The RFI mitigation with auxiliary beams is successful. If the interferer is below the noise floor (RNR $<$ 0 dB), the filtering introduces a degradation as discussed before. It can be observed that the degradation (when the method is applied in the absence of detectable RFI) increases with the SNR but is negligible for SNR $=$ 0 dB. This is the case because the notched but correlated SAR signal has no effect for SNR $=$ 0 dB. For large SNR values, the behavior approaches the noiseless case in Fig. 15(a).

Nevertheless, the system could avoid the performance degradation with a simple thresholding of k.

1) Effect of LMS Filter Length on Mitigation Performance: The estimation of k with an LMS filter requires the selection of a filter length. The concept for this estimation was introduced in Section II-C and assumed that k is approximately constant in azimuth, an assumption that only holds for a few hundred pulses and depends on the beamwidth in azimuth. Table II summarizes the maximum residual error for RNR $>$ 0 dB in dependence of the LMS filter length. An increase in the error with decreasing filter length is evident, because the filter becomes more susceptible to noise. Hence, while shorter filters are desirable for an assumption of a constant k, the minimum length needs to account for the impact of noise. In addition to this, the filter length will also need to be set angle dependently for a reflector antenna, when the relative antenna pattern change within the filter cannot be neglected.

TABLE II

MAXIMUM RESIDUAL ERROR INCREASE AFTER RFI MITIGATION FOR RNR $>$ 0 dB. THE VALUES IN PARENTHESES ARE FOR SNR $>$ 20 dB

	500 pulses	**300 pulses**	**100 pulses**
Phase Std. Dev. [deg]	0.2	0.4	1.5
Phase Offset [deg]	0.04	0.05	0.24
Amplitude Offset [dB]	0.01	0.01	0.04
Amplitude Std. Dev. [dB]	0.58 (0.03)	0.44 (0.03)	4.4 (0.03)

TABLE III

MAXIMUM RESIDUAL ERROR INCREASE AFTER RFI MITIGATION FOR RNR $<$0 dB. THE VALUES IN PARENTHESES ARE FOR SNR $>$ 20 dB

	500 pulses	**300 pulses**	**100 pulses**
Phase Std. Dev. [deg]	1.8 (17.2)	3.0 (22.1)	8.3 (37.3)
Phase Offset [deg]	0.4 (1.8)	0.49 (3.0)	1.9 (8.2)
Amplitude Offset [dB]	0.06 (0.39)	0.1 (0.6)	0.34 (1.6)
Amplitude Std. Dev. [dB]	1.0 (19.6)	1.1 (21.3)	2.9 (27.2)

Next, Table III summarizes the maximum error degradation for RNR $<$ 0 dB. Again, the error increases for shorter filter

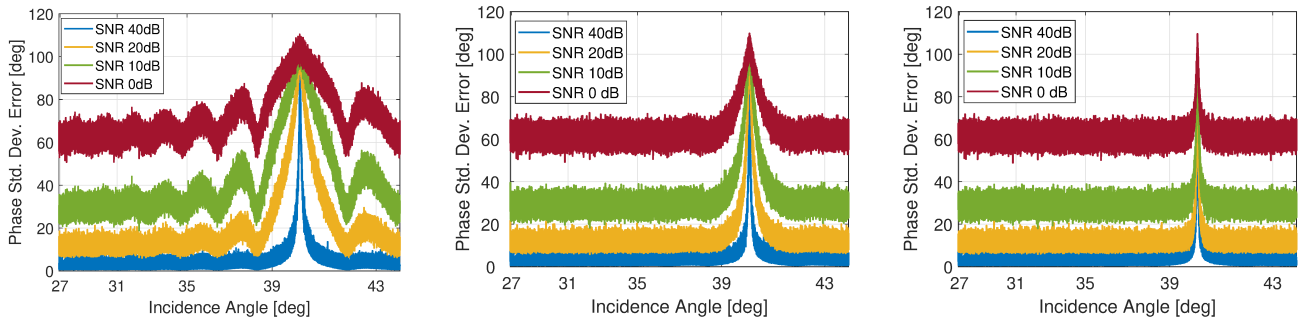

Fig. 16. Phase standard deviation error for an in-swath interferer ($\theta_{\mathrm{I}} = 40°$ and baseband frequency $f_{\mathrm{RFI}} = 25$ MHz) at RSR = 64 dB (the RSR level is chosen to better demonstrate the shown effect). The auxiliary beam is formed as (a) wide beam, (b) wide beam with frequency bandpass for noise reduction, and (c) narrow beam with frequency bandpass filter.

lengths. While the amplitude offset increase for SNR > 20 dB is small for a reduction from 500 pulses to 300 pulses (0.39–0.6 dB), the error increases significantly for 100 pulses (1.6 dB). Errors of this magnitude affect the radiometric budget. The other error parameters show a good performance. This means a short filter window can only be implemented if the system applies a thresholding of k.

D. Simulation Results for In-Swath RFI

Section VII-C demonstrated the out-of-swath interference mitigation performance of the simulated system, which uses auxiliary beams. This section places an interferer inside the system's swath at $\theta_{\mathrm{I}} = 35.13°$ (40° incidence angle) and investigates the impact on the mitigation performance.

Fig. 16 shows the residual phase standard deviation error due to the in-swath interferer (RSR = 64 dB) for a CW RFI signal transmitted at a baseband frequency of $f_{\mathrm{RFI}} = 25$ MHz. The system uses a wide auxiliary beam in the first plot [Fig. 16(a)]. The interference is removed from the data as long as the instantaneous radar return and the RFI signal are spatially separated; otherwise, a residual error occurs when the auxiliary beam and the SCORE beam overlap and thus the error peaks for an incidence angle of $\theta_{\mathrm{i}} = 40°$. However, the error is already noticeable at $\theta_{\mathrm{i}} = 34°$. The SNR in the wide auxiliary beam is N times lower than in the SCORE beam, and thus this approach is limited for measuring weak RFI (Section III-A, the spatial resolution in a DBF system improves with the SNR). Therefore, the performance degradation is worse at SNR = 0 dB than at SNR = 40 dB.

This effect is reduced by bandpass-filtering the wide auxiliary beam in the frequency domain and results are shown in Fig. 16(b). As discussed in Section III-A, the bandpass reduces the noise power in the auxiliary beam and thus achieves a better spatial resolution by means of a smaller resolution factor ζ (13). The performance degradation for SNR = 0 dB does not appear until $\theta_{\mathrm{i}} = 39°$, because less RFI information is lost in the auxiliary beam.

Switching the system from a wide auxiliary beam to a focused auxiliary beam further lowers ζ and the size of the expected estimation gap. This is shown in Fig. 16(c) (with bandpass). The peak of the residual error is narrow for all plotted SNR levels, which is favorable for a removal of in-swath interference by modeling the estimation gap as was discussed in Section IV and will be simulated in Section VII-E.

E. Simulation of the Estimation Gap Reconstruction

As seen in Section VII-D, a main limitation of DBF-based RFI mitigation methods is that they are incapable of filtering in-swath interferers[3] while the SCORE beam is looking into the direction of RFI. This section reconstructs the lost RFI signal with an autoregressive model (Burg's method), which allows for a removal of the residual error peak. The result of this approach depends on the length of the estimation gap t_{gap} as well as on the stationarity of the interference over this time period.

Two different types of RFI signals are considered. First, the impact of a CW signal at a baseband frequency of $f_{\mathrm{RFI}} = 25$ MHz is studied in VII-E1. Next, the impact of a random BFSK signal is analyzed in VII-E2. The residual 3-sigma phase standard deviation errors after gap reconstruction with different window sizes are presented. Note that results for the remaining error parameters (phase offset, amplitude offset, and amplitude standard deviation) can be found in [61].

1) CW-Signal: The residual phase standard deviation error results for the CW interferer are shown in Fig. 17 for SNR = 40 dB. Fig. 17(a) shows the residual error that remains after LMS and bandpass filtering (before the estimation gap is reconstructed). The results are plotted versus fast time ($\tau = 0$ corresponds to the SCORE beam pointing directly at the interferer) and the corrupted gap is visible for RNR values above 14 dB. As the RNR increases, the leakage effect of the fast Fourier transform (FFT) requires the use of a wider bandpass filter, which results in a larger resolution factor ζ and a widening of the estimation gap. The same effect is visible for SNR = 0 dB in Fig. 18(a). Here, the widening of the

[3]Conventional RFI mitigation methods are able to remove neither in-swath interference nor out-of-swath interference without introducing significant drawbacks.

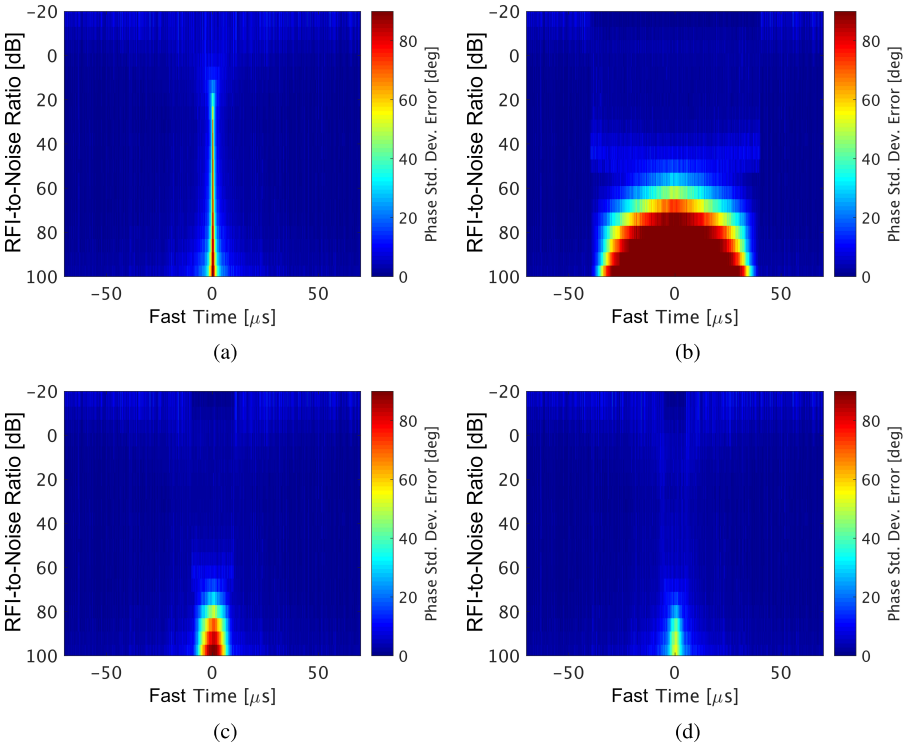

Fig. 17. Phase standard deviation error versus fast time (centered on the interferer position) dependent on RNR (SNR = 40 dB). (a) No autoregressive model (LMS and bandpass only). (b) Autoregressive model applied over 80 μs window. (c) Autoregressive model applied over 20 μs window. (d) Autoregressive model applied over 10 μs window.

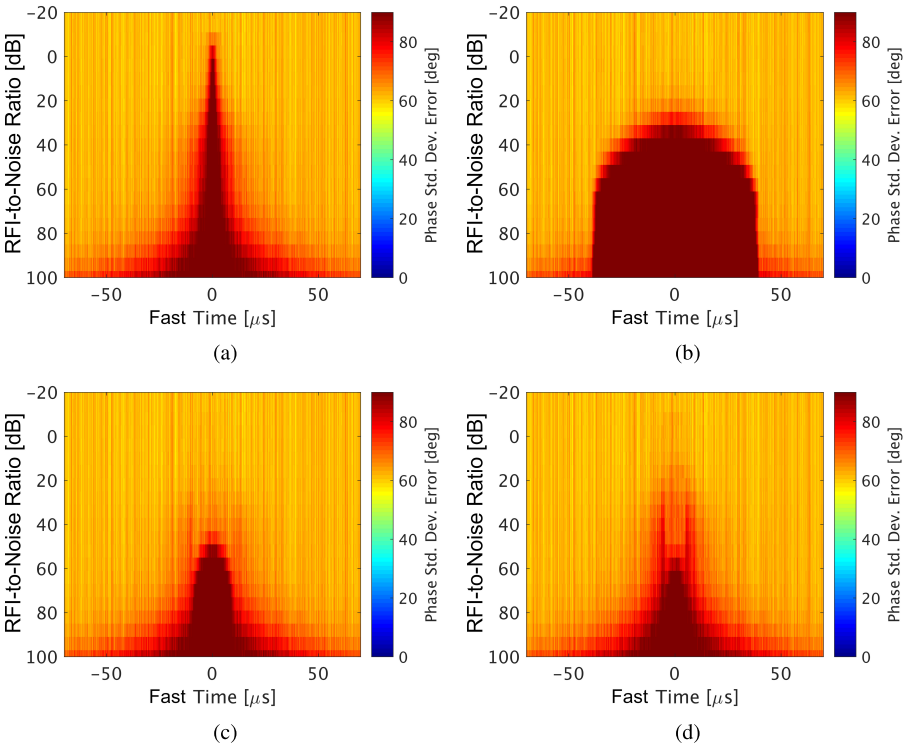

Fig. 18. Phase standard deviation error versus fast time (centered on interferer position) dependent on RNR (SNR = 0 dB). (a) No autoregressive model (LMS and bandpass only). (b) Autoregressive model applied over 80 μs window. (c) Autoregressive model applied over 20 μs window. (d) Autoregressive model applied over 10 μs window.

estimation gap for larger RNR is more pronounced, because the performance at low SNR is more sensitive to changes of ζ and thus the degradation already starts at an RNR of -14 dB.

Next, the estimation gap is reconstructed in an 80 μs estimation window centered on the interferer position ($\tau = 0$). The residual error after the gap reconstruction is shown in

Figs. 17(b) and 18(b) for SNR = 40 dB and SNR = 0 dB, respectively. In both the cases, the first RNR value with residual errors is 40 dB larger than without the gap modeling and hence 40-dB stronger RFI can be fully removed. This comes at the cost of a sudden degradation for larger RNR values. When the gap reconstruction fails, the entire 80 μs in the estimation window are lost. The performance at large RNR is worse than without gap modeling and can be explained by the leakage effect of the FFT. Because the bandpass filter widens with RNR, the stationarity duration of the signal is reduced. Shorter estimation windows are necessary to remove stronger RFI. This is in agreement with the results simulated for SNR = 40 dB using estimation windows of 20 and 10 μs in Fig. 17(c) and (d), respectively. The shorter the estimation window, the wider the acceptable bandpass filter and thus the greater the acceptable RNR values. For SNR = 40 dB, the RNR values of larger than 80 dB could theoretically be filtered, although such large values will exceed the common dynamic range of SAR systems and thus saturate the receiver—resulting in an irreversible loss of the data.

The results for SNR = 0 dB are shown in Fig. 18(c) and (d). Here, it is evident that the smallest estimation window size is limited by the noise scaling constraint: there is no improvement between the 20- and 10-μs estimation windows. The smaller estimation window actually performs worse once the estimation window is smaller than the actual estimation gap. Nevertheless, even a low SNR allows the removal of RNR up to 50 dB.

It is worth noting that this gap reconstruction is not performed on-board itself. Instead, it is performed on ground and the estimation window length can be optimized after data acquisition.

Fig. 19(a) represents the results of Figs. 17 and 18 in 1-D plots. The plots show the 3-sigma phase standard deviation increase computed over an 80 μs window centered on the interferer position ($\tau = 0$) versus RNR. For high SNR (Fig. 19), a reduction of the estimation window length moves the critical RNR from the previously mentioned 14 dB (without gap modeling) to a value of about 80 dB. For low SNR [Fig. 19(b)], an improvement is only visible for shrinking the estimation window to 20 μs. The degradation of the reconstruction for smaller estimation windows is visible in the 1-D plot. The gap modeling sufficiently suppresses RFI in the system up to a critical RNR of about 50 dB.

2) Random BFSK-Signal: In this section, the emitted RFI signal is a random communication signal encoded with a BFSK modulation with symbol length S_L. A random discrete vector v with uniformly distributed ones and zeros is simulated. The vector is then modulated onto the frequencies f_1 and f_2. The resulting RFI signal shifts between both the frequencies and is given by

$$r(\tau, t) = e^{j2\pi f_{\mathrm{RFI}}(\tau,t)(t+\tau+t_{\mathrm{offset}}(p))} \tag{32}$$

with the imaginary unit j and

$$f_{\mathrm{RFI}}(\tau, t) = \begin{cases} f_1 \colon v\left(\left\lfloor \dfrac{t+\tau+t_{\mathrm{offset}}(p)}{S_L} \right\rceil\right) = 0 \\ f_2 \colon v\left(\left\lfloor \dfrac{t+\tau+t_{\mathrm{offset}}(p)}{S_L} \right\rceil\right) = 1. \end{cases} \tag{33}$$

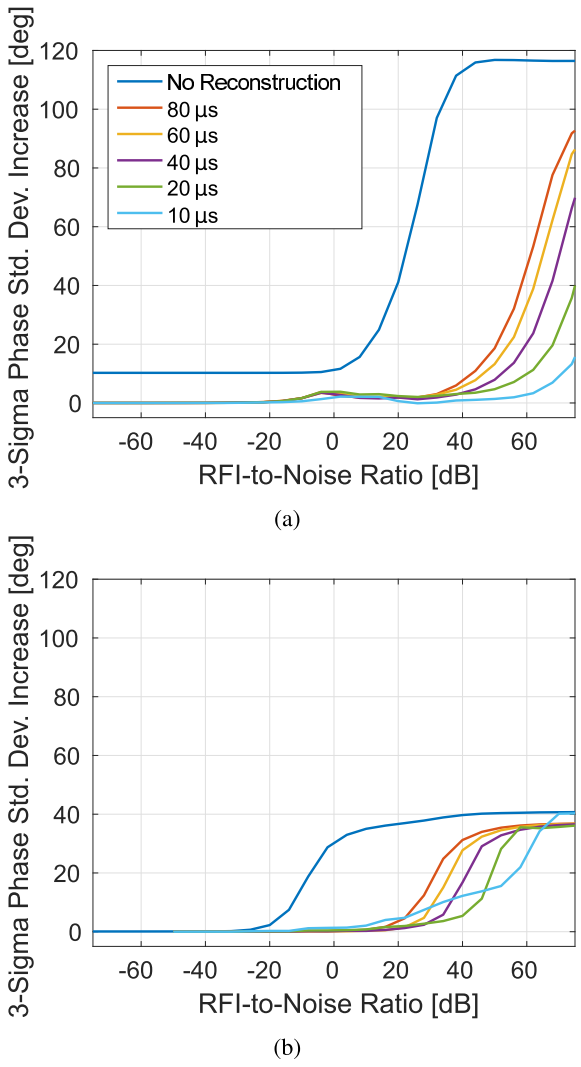

Fig. 19. 3-sigma phase std. dev. increase computed in 80 μs window centered on the CW interferer position for (a) SNR = 40 dB and (b) SNR = 0 dB.

The start position of a symbol within each receive window p is varied with a random offset $t_{\mathrm{offset}}(p)$. The carrier frequencies are set to $f_1 = 25$ MHz and $f_2 = 27$ MHz in baseband. Even though a realistic spacing is expected to be smaller than 2 MHz, this large spacing is selected to reduce the similarity between symbols. The resulting RFI signal is random in the azimuth direction and thus will demonstrate the capabilities of a system using the proposed RFI mitigation method. The symbol length S_L is set to 150, 80, and 40 μs, resulting in three separate simulation scenarios. As the symbol length is shortened, the stationarity of the RFI signal is decreased (increased RFI bandwidth) and this is expected to impact the gap modeling performance with the autoregressive model. Therefore, the longest selected symbol length ($S_L = 150$ μs) should result in the best reconstruction.

The 3-sigma phase standard deviation increase computed over a 80 μs window centered on the BFSK interferer position is shown in Fig. 20.

For $S_L = 150$ μs and SNR = 40 dB, the error increase stays below 10° for the RNR values of up to 55 dB. For SNR = 0 dB, the error increase stays below 10° for the RNR values of

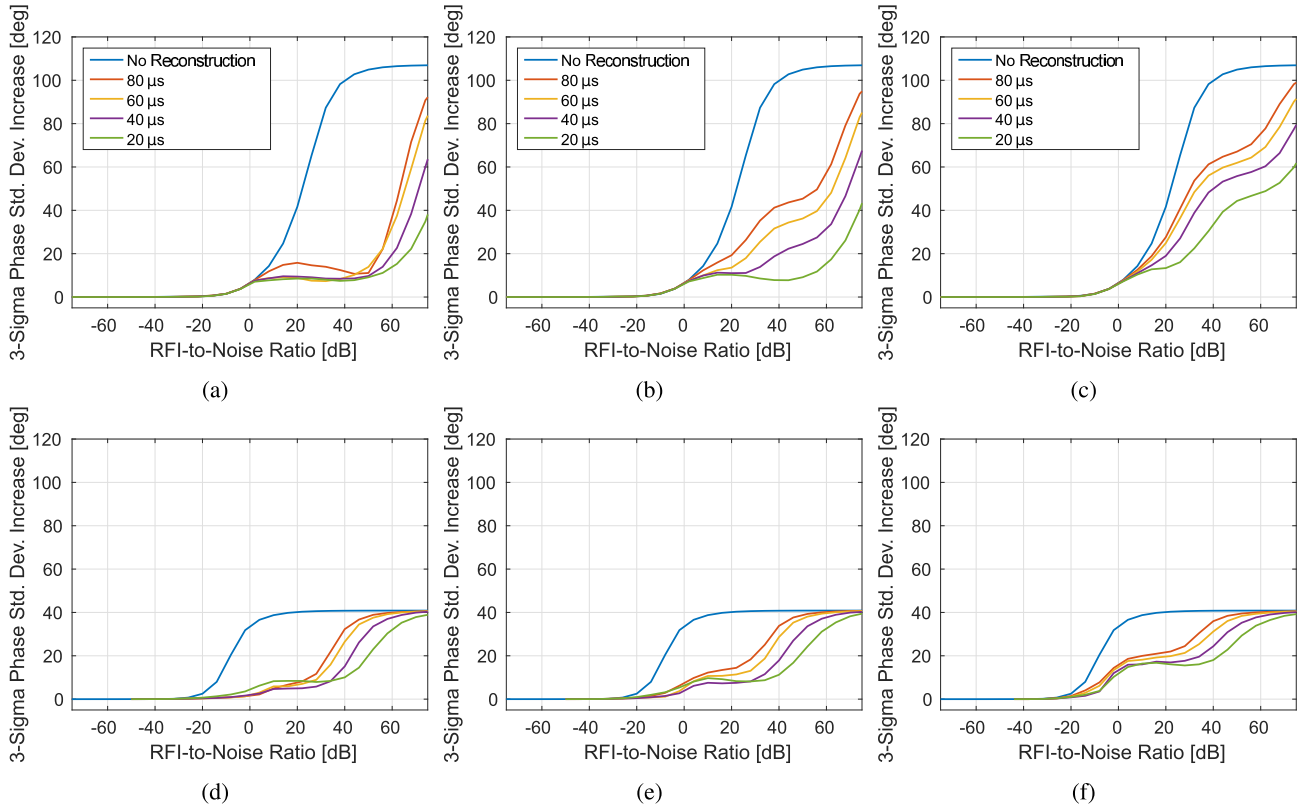

Fig. 20. 3-sigma phase std. dev. increase computed in 80 μs window centered on the BFSK interferer position. (a) $S_L = 150$ μs; SNR $= 40$ dB. (b) $S_L = 80$ μs; SNR $= 40$ dB. (c) $S_L = 40$ μs; SNR $= 40$ dB. (d) $S_L = 150$ μs; SNR $= 0$ dB. (e) $SL = 80$ μs; SNR $= 0$ dB. (f) $S_L = 40$ μs, SNR $= 0$ dB.

up to 40 dB. This is about twice the phase standard deviation error caused by a continuous interferer at these RNR and SNR levels. Similar values can be seen for $S_L = 80$ μs, though a worsening of the performance for larger estimation windows is noticeable. However, for $S_L = 40$ μs, the performance drops. The RNR thresholds are lowered to 8 and -2 dB for SNR $=$ 40 dB and SNR $= 0$ dB, respectively. While the gap modeling does improve the signal, it is not able to fully recover the image quality.

VIII. Conclusion and Outlook

The new baseline for SAR-based Earth observation is multichannel radars capable of DBF, which can spatially filter interference independent of the RFI signal properties. In this article, we proposed a novel DBF-based method that moves the RFI mitigation to the on-ground processing chain without the need to downlink all channels. The reduction of the data volume is achieved by means of a spatial prefiltering on-board with auxiliary beams. These auxiliary beams are synthesized simultaneously with the SCORE beam, use the same antenna, and point toward the RFI sources. In this way, information on the RFI is collected while simultaneously suppressing the instantaneous SAR echo signal with a time-dependent antenna pattern notch. The RFI information is downlinked and coherently subtracted from the data. For this purpose, different implementations of the auxiliary beam were proposed along with an LMS filter that optimizes the subtraction.

As with all spatial filtering methods, the mitigation only works while the RFI and SAR signals can be separated. A theoretical examination, supplemented by the simulation of a DBF system using the proposed method, showed that the amount of lost RFI information—due to the spatial overlap—is controlled by system design parameters, such as antenna size and the number of receive channels, but can also be reduced by oversampling and bandpass filtering the auxiliary beams.

In addition, this article presented a new approach to recover the lost RFI information solely by modeling the interference based on the information available in the auxiliary beams. The performance of this innovative reconstruction was simulated using an autoregressive model and showed that this method can fully remove in-swath interferers, as well, provided the interference is stationary for the duration of the lost RFI signal.

Future studies could improve the reconstruction by applying more sophisticated models to the auxiliary beam data. Such models could, for example, use pattern recognition for periodical RFI signals or decode the received symbols in order to predict the symbols lost inside of the estimation gap. In addition, the on-ground scaling coefficient estimation could be enhanced with *a priori* knowledge of the antenna pattern and interferer position.

References

[1] J. C. Curlander and R. N. McDonough, *Synthetic Aperture Radar: Systems and Signal Theory*. Hoboken, NJ, USA: Wiley, 1991.

[2] F. Ulaby, M. C. Dobson, and J. L. Álvarez-Pérez, *Handbook of Radar Scattering Statistics for Terrain*. Norwood, MA, USA: Artech House, 2019.

[3] H. Mazar, *Radio Spectrum Management: Policies, Regulations and Techniques*. Hoboken, NJ, USA: Wiley, 2016.

[4] National Academies of Sciences, Engineering, and Medicine, *A Strategy for Active Remote Sensing Amid Increased Demand for Radio Spectrum*. Washington, DC, USA: National Academies Press, 2015.

[5] A. Monti-Guarnieri, D. Giudici, and A. Recchia, "Identification of C-band radio frequency interferences from Sentinel-1 data," *Remote Sens.*, vol. 9, no. 11, p. 1183, Nov. 2017.

[6] P. A. Rosen, S. Hensley, and C. Le, "Observations and mitigation of RFI in ALOS PALSAR SAR data: Implications for the DESDynI mission," in *Proc. IEEE Radar Conf.*, May 2008, pp. 1–6.

[7] F. J. Meyer, J. B. Nicoll, and A. P. Doulgeris, "Correction and characterization of radio frequency interference signatures in L-band synthetic aperture radar data," *IEEE Trans. Geosci. Remote Sens.*, vol. 51, no. 10, pp. 4961–4972, Apr. 2013.

[8] F. J. Meyer, J. B. Nicoll, and A. P. Doulgeris, "Characterization and extent of randomly-changing radio frequency interference in ALOS PALSAR data," in *Proc. IEEE Int. Geosci. Remote Sens. Symp.*, Jul. 2011, pp. 2448–2451.

[9] M. Spencer and F. Ulaby, "Spectrum issues faced by active remote sensing: Radio frequency interference and operational restrictions technical committees," *IEEE Geosci. Remote Sens. Mag.*, vol. 4, no. 1, pp. 40–45, Mar. 2016.

[10] E. Stofan *et al.*, "Overview of results of spaceborne imaging radar-C, X-band synthetic aperture radar (SIR-C/X-SAR)," *IEEE Trans. Geosci. Remote Sens.*, vol. 33, no. 4, pp. 817–828, Jul. 1995.

[11] T. Bollian, B. Osmanoglu, R. F. Rincon, S.-K. Lee, and T. E. Fatoyinbo, "Detection and geolocation of P-band radio frequency interference using EcoSAR," *IEEE J. Sel. Topics Appl. Earth Observ. Remote Sens.*, vol. 11, no. 10, pp. 3608–3616, Oct. 2018.

[12] J. M. B. Carreiras *et al.*, "Coverage of high biomass forests by the ESA BIOMASS mission under defense restrictions," *Remote Sens. Environ.*, vol. 196, pp. 154–162, Jul. 2017.

[13] D. Giudici, P. Guccione, D. Geudtner, and R. Torres, "RLAN impact on Sentinel-1 C-band SAR performance," in *Proc. 12th Eur. Conf. Synth. Aperture Radar (EUSAR)*, Jun. 2018, pp. 1–6.

[14] *Radio Regulations*, ITU, Geneva, Switzerland, 2016.

[15] R. T. Lord and M. R. Inggs, "Approaches to RF interference suppression for VHF/UHF synthetic aperture radar," in *Proc. South Afr. Symp. Commun. Signal Process. (COMSIG)*, Sep. 1998, pp. 95–100.

[16] W. Chang, J. Li, and X. Li, "The effect of notch filter on RFI suppression," *Wireless Sensor Netw.*, vol. 1, no. 3, pp. 196–205, 2009.

[17] A. Reigber and L. Ferro-Famil, "Interference suppression in synthesized SAR images," *IEEE Geosci. Remote Sens. Lett.*, vol. 2, no. 1, pp. 45–49, Jan. 2005.

[18] N. Li, Z. Lv, Z. Guo, and J. Zhao, "Time-domain notch filtering method for pulse RFI mitigation in synthetic aperture radar," *IEEE Geosci. Remote Sens. Lett.*, vol. 19, pp. 1–5, 2021.

[19] W. Xu, W. Xing, C. Fang, P. Huang, and W. Tan, "RFI suppression based on linear prediction in synthetic aperture radar data," *IEEE Geosci. Remote Sens. Lett.*, vol. 18, no. 12, pp. 2127–2131, Dec. 2021.

[20] A. Potsis, A. Reigber, and K. P. Papathanassiou, "A phase preserving method for RF interference suppression in P-band synthetic aperture radar interferometric data," in *Proc. Int. Geosci. Remote Sens. Symp.*, vol. 5, 1999, pp. 2655–2657.

[21] M. Braunstein, J. M. Ralston, and D. A. Sparrow, "Signal processing approaches to radio frequency interference (RFI) suppression," *Proc. SPIE*, vol. 2230, pp. 190–208, Apr. 1994.

[22] R. T. Lord and M. R. Inggs, "Efficient RFI suppression in SAR using LMS adaptive filter integrated with range/Doppler algorithm," *Electron. Lett.*, vol. 35, no. 8, pp. 629–630, Apr. 1999.

[23] C. T. C. Le, S. Hensley, and E. Chapin, "Removal of RFI in wideband radars," in *Proc. Geosci. Remote Sens. Symp.*, vol. 4, Jul. 1998, pp. 2032–2034.

[24] W. Fan *et al.*, "Interference mitigation for synthetic aperture radar based on deep residual network," *Remote Sens.*, vol. 11, no. 14, p. 1654, Jul. 2019.

[25] H. Zhang, Y. Huang, J. Li, Z. Chen, L. Cai, and W. Hong, "Time-varying RFI mitigation for SAR systems via graph Laplacian clustering techniques," *IEEE Geosci. Remote Sens. Lett.*, vol. 19, pp. 1–5, 2021.

[26] F. Zhou, M. Tao, X. Bai, and J. Liu, "Narrow-band interference suppression for SAR based on independent component analysis," *IEEE Trans. Geosci. Remote Sens.*, vol. 51, no. 10, pp. 4952–4960, Oct. 2013.

[27] P. Comon and C. Jutten, *Handbook of Blind Source Separation: Independent Component Analysis and Applications*. New York, NY, USA: Academic, 2010.

[28] S. Applebaum, "Adaptive arrays," *IEEE Trans. Antennas Propag.*, vol. AP-24, no. 5, pp. 585–598, Sep. 1976.

[29] A. Farina, "Single sidelobe canceller: Theory and evaluation," *IEEE Trans. Aerosp. Electron. Syst.*, vol. AES-13, no. 6, pp. 690–699, Nov. 1977.

[30] A. Farina and F. A. Studer, "Evaluation of sidelobe-canceller performance," *IEE Proc. F, Commun., Radar Signal Process.*, vol. 129, no. 1, pp. 52–58, Feb. 1982.

[31] M. Sedehi, D. Cristallini, J. Marini, and P. Lombardo, "Impact of an electromagnetic interference on imaging capability of a synthetic aperture radar," in *Proc. IEEE Aerosp. Conf.*, Mar. 2007, pp. 1–8.

[32] M. Sedehi, F. Colone, D. Cristallini, and P. Lombardo, "A reduced order jammer cancellation scheme based on double adaptivity," in *Proc. IEEE Radar Conf.*, May 2008, pp. 1–6.

[33] P. Lombardo, M. Sedehi, F. Colone, M. Bucciarelli, and D. Cristallini, "Dual channel adaptive antenna nulling with auxiliary selection for spaceborne radar," in *Proc. IEEE Aerosp. Conf.*, Mar. 2008, pp. 1–8.

[34] M. Sedehi, D. Cristallini, M. Bucciarelli, and P. Lombardo, "Constrained adaptive beamforming for electromagnetic interference cancellation for a synthetic aperture radar," in *Proc. IET Int. Conf. Radar Syst.*, Oct. 2007, pp. 1–5.

[35] T. Bollian, B. Osmanoglu, R. Rincon, S.-K. Lee, and T. Fatoyinbo, "Adaptive antenna pattern notching of interference in synthetic aperture radar data using digital beamforming," *Remote Sens.*, vol. 11, no. 11, p. 1346, Jun. 2019.

[36] M. Younis, C. Fischer, and W. Wiesbeck, "Digital beamforming in SAR systems," *IEEE Trans. Geosci. Remote Sens.*, vol. 41, no. 7, pp. 1735–1739, Jul. 2003.

[37] A. Moreira *et al.*, "Tandem-L: A highly innovative bistatic SAR mission for global observation of dynamic processes on the Earth's surface," *IEEE Geosci. Remote Sens. Mag.*, vol. 3, no. 2, pp. 8–23, Jun. 2015.

[38] P. Rosen *et al.*, "An update on the NASA-ISRO dual-frequency DBF SAR (NISAR) mission," in *Proc. IEEE Int. Geosci. Remote Sens. Symp. (IGARSS)*, Jul. 2016, pp. 2106–2108.

[39] M. Konaka, T. Motohka, K. Yamamoto, Y. Kankaku, Y. Arikawa, and S. Suzuki, "Current status of developing ALOS-4 with key missions: PALSAR-3 and SPAISE3," in *Proc. IEEE Int. Geosci. Remote Sens. Symp. IGARSS*, Jul. 2021, pp. 387–390.

[40] N. Pierdicca *et al.*, "The copernicus L-band SAR mission ROSE-L (radar observing system for Europe)(conference presentation)," *Proc. SPIE*, vol. 11154, Oct. 2019, Art. no. 111540E.

[41] M. Zonno *et al.*, "Sentinel-1 next generation: Trade-offs and assessment of mission performance," in *Proc. ESA Living Planet Symp.*, Milan, Italy, May 2019.

[42] G. Krieger, N. Gebert, and A. Moreira, "Digital beamforming techniques for spaceborne radar remote sensing," in *Proc. Eur. Conf. Synth. Aperture Radar (EUSAR)*. Berlin, Germany: VDE Verlag GmbH, 2006, pp. 1–4.

[43] B. D. Van Veen and K. M. Buckley, "Beamforming: A versatile approach to spatial filtering," *IEEE ASSP Mag.*, vol. 5, no. 2, pp. 4–24, Apr. 1988.

[44] M. Suess, B. Grafmueller, and R. Zahn, "A novel high resolution, wide swath SAR system," in *Proc. Scanning Present Resolving Future, Int. Geosci. Remote Sens. Symp. (IGARSS)*, vol. 3, Aug. 2001, pp. 1013–1015.

[45] M. Younis, T. Rommel, F. Bordoni, G. Krieger, and A. Moreira, "On the pulse extension loss in digital beamforming SAR," *IEEE Geosci. Remote Sens. Lett.*, vol. 12, no. 7, pp. 1436–1440, Jul. 2015.

[46] M. Suess and W. Wiesbeck, "Side-looking synthetic aperture radar system," European Patent 1 241 487 B1, Sep. 2002.

[47] G. Krieger *et al.*, "CEBRAS: Cross elevation beam range ambiguity suppression for high-resolution wide-swath and MIMO-SAR imaging," in *Proc. IEEE Int. Geosci. Remote Sens. Symp. (IGARSS)*, Jul. 2015, pp. 196–199.

[48] G. Strang, *Introduction to Linear Algebra*. Wellesley, MA, USA: Wellesley-Cambridge Press, 1993.

[49] T. L. Lai, H. Robbins, and C. Z. Wei, "Strong consistency of least squares estimates in multiple regression," *Proc. Nat. Acad. Sci. USA*, vol. 75, no. 7, p. 3034, 1978.

[50] A. Moreira, "Radar mit synthetischer Apertur," Habilitation, Universitaet Fridericiana zu Karlsruhe, 1999.
[51] R. Steele and F. Benjamin, "Sample reduction and subsequent adaptive interpolation of speech signals," *Bell Labs Tech. J.*, vol. 62, no. 6, pp. 1365–1398, 1983.
[52] A. Janssen, R. Veldhuis, and L. Vries, "Adaptive interpolation of discrete-time signals that can be modeled as autoregressive processes," *IEEE Trans. Acoust., Speech, Signal Process.*, vol. ASSP-34, no. 2, pp. 317–330, Apr. 1986.
[53] S. V. Vaseghi and P. J. W. Rayner, "A new application of adaptive filters for restoration of archived gramophone recordings," in *Proc. Int. Conf. Acoust., Speech, Signal Process.*, 1988, pp. 2548–2551.
[54] S. Godsill, P. Rayner, and O. Cappé, "Digital audio restoration," in *Applications of Digital Signal Processing to Audio and Acoustics*. Berlin, Germany: Springer-Verlag, 2002, pp. 133–194.
[55] J. P. Burg, "Maximum entropy spectral analysis," in *Proc. 37th Annu. Int. Meeting, Soc. Explor. Geophys.*, Oklahoma City, OK, Oct. 1967.
[56] R. Shibata, "Selection of the order of an autoregressive model by Akaike's information criterion," *Biometrika*, vol. 63, no. 1, pp. 117–126, 1976.
[57] M. B. Priestley, *Spectral Analysis and Time Series*. New York, NY, USA: Academic, 1981.
[58] M. J. L. de Hoon, T. H. J. J. van der Hagen, H. Schoonewelle, and H. van Dam, "Why Yule–Walker should not be used for autoregressive modelling," *Ann. Nucl. Energy*, vol. 23, no. 15, pp. 1219–1228, 1996.
[59] C. Collomb, "Burg's method, algorithm and recursion," *Comput. Sci.*, Nov. 2009. [Online]. Available: http://ccollomb.free.fr/ and https://www.academia.edu/36134729/Burgs_Method_Algorithm_and_Recursion
[60] *National Association for Amateur Radio*. Accessed: Oct. 2019. [Online]. Available: http://www.arrl.org/modes-systems
[61] T. Bollian, "Digital beamforming for radio frequency interference suppression in synthetic aperture radar," Ph.D. dissertation, Karlsruhe Inst. Technol., Karlsruhe, Germany, 2019. [Online]. Available: https://elib.dlr.de/130454/
[62] C. Balanis, *Antenna Theory*. New York, NY, USA: Wiley, 1997.

Tobias Bollian (Member, IEEE) received the B.Sc., M.Sc., and Ph.D. degrees in electrical engineering from the Karlsruhe Institute of Technology, Karlsruhe, Germany, in 2012, 2014, and 2019, respectively.

In 2013, he was a Student Researcher with the Alaska Satellite Facility, Fairbanks, AK, USA. From 2014 to 2015, he was with the European Space Agency's (ESA's) European Space Research and Technology Center, Noordwijk, The Netherlands, under the Young Graduate Trainee Program. From 2015 to 2019, he was an Associate Scientist with the Biospheric Sciences Laboratory, NASA Goddard Space Flight Center, Greenbelt, MD, USA, where he worked on digital-beamforming-based RFI mitigation techniques for synthetic aperture radar (SAR). Since 2019, he has been with the Microwaves and Radar Institute, German Aerospace Center (DLR), Wessling, Germany. His research interests include active microwave remote sensing, with special interest in SAR signal processing, performance simulation, digital beamforming, and radio frequency interference mitigation.

Dr. Bollian is a member of the IEEE Geoscience and Remote Sensing Society and a Co-Chair of the IEEE Geoscience and Remote Sensing Society (GRSS) Frequency Allocations in Remote Sensing Technical Committee.

Marwan Younis (Fellow, IEEE) received the B.Sc. degree in electrical engineering from the University of Baghdad, Baghdad, Iraq, in 1992, and the Dipl.-Ing. (M.Sc.) and Dr.-Ing. (Ph.D.) degrees in electrical engineering from the Universität Karlsruhe (TH), Karlsruhe, Germany, in 1997 and 2004, respectively.

From 1998 to 2004, he was a Research Scientist with the Institut für Höchstfrequenztechnik und Elektronik, Universität Karlsruhe. Since 2005, he has been with the German Aerospace Center (DLR), Microwaves and Radar Institute, Wessling. He is the Head of the SAR Techniques Group, DLR, and a Professor of spaceborne radar systems with the Karlsruhe Institute for Technology (KIT), Karlsruhe. He has authored or coauthored about 190 conference papers, 45 reviewed publications, and holds five patents. His research fields include synthetic aperture radar (SAR) systems and techniques, multiple input multiple output (MIMO) SAR, digital beamforming, SAR performance, calibration, and antennas. In 1996, he was an Intern with the Jet Propulsion Laboratory (JPL), Pasadena, CA, USA, in 2013 and 2019, where he spent research sabbaticals.

Dr. Younis is an Active Member of Geoscience and Remote Sensing Society (GRSS). He served GRSS AdCom from 2018 to 2020. He received the Hermann-Billing Award for his Ph.D. thesis in 2005 and was awarded the title DLR Senior Scientist in 2021. He is the Co-Chair of the Instrumentation and Future Technologies GRSS Technical Committee. He is a reviewer of IEEE publications and was an Associate Editor of the IEEE GEOSCIENCE AND REMOTE SENSING LETTER from 2012 to 2019.

Gerhard Krieger (Fellow, IEEE) received the Dipl.-Ing. (M.S.) and Dr.-Ing. (Ph.D.) (Hons.) degrees in electrical and communication engineering from the Technical University of Munich, Munich, Germany, in 1992 and 1999, respectively.

From 1992 to 1999, he was with the Ludwig Maximilians University, Munich, where he conducted multidisciplinary research on neuronal modeling and nonlinear information processing in biological and technical vision systems. Since 1999, he has been with the German Aerospace Center (DLR), Microwaves and Radar Institute, Wessling, Germany, where he started as a Research Associate developing signal processing algorithms for a novel forward-looking radar system employing digital beamforming on receive. From 2001 to 2007, he led the New SAR Missions Group which pioneered the development of advanced bistatic and multistatic radar systems, such as TanDEM-X, as well as innovative multichannel SAR techniques and algorithms for high-resolution wide-swath (HRWS) SAR imaging. Since 2008, he has been the Head of the Radar Concepts Department which hosts about 40 scientists focusing on new SAR techniques, missions, and applications. He has been serving as the Mission Engineer for TanDEM-X and he made also major contributions to the development of the Tandem-L mission concept, where he led the Phase-0 and Phase-A studies. Since 2019, he has been holding a Professorship with the Friedrich-Alexander-University Erlangen, Erlangen, Germany. He has authored or coauthored more than 100 peer-reviewed journal articles, nine invited book chapters, more than 400 conference papers, and more than 20 patents.

Prof. Krieger received several national and international awards, including the two Best Paper Awards at the European Conference on SAR, the two Transactions Prize Paper Awards of the IEEE Geoscience and Remote Sensing Society, and the W. R. G. Baker Prize Paper Award from the IEEE Board of Directors. He has been an Associate Editor for the IEEE TRANSACTIONS ON GEOSCIENCE AND REMOTE SENSING since 2012. In 2014, he served as the Technical Program Chair for the European Conference on Synthetic Aperture Radar (SAR) and as a Guest Editor for the IEEE JOURNAL OF SELECTED TOPICS IN APPLIED EARTH OBSERVATIONS AND REMOTE SENSING.

Alberto Moreira (Fellow, IEEE) received the B.S.E.E. and M.S.E.E. degrees from the Aeronautical Technological Institute (ITA), São José dos Campos, Brazil, in 1984 and 1986, respectively, and the Dr.Eng. degree (Hons.) from the Technical University of Munich, Munich, Germany, in 1993.

From 1996 to 2001, he was the Head of the SAR Technology Department, German Aerospace Center (DLR), Wessling, Germany. Under his leadership, the DLR airborne SAR system has been upgraded to operate in innovative imaging modes, such as polarimetric SAR interferometry, tomography, and holography. Since 2001, he has been the Director of the Microwaves and Radar Institute, DLR, and a Full Professor with the Karlsruhe Institute of Technology (KIT), in the field of microwave remote sensing. His DLR's Institute contributes to several scientific programs and projects for Spaceborne SAR Missions such as TerraSAR-X, TanDEM-X, high resolution wide swath (HRWS), SAR-Lupe, and SARah as well as Kompsat-6, PAZ, Sentinel-1, BIOMASS, ROSE-L, Harmony, Sentinel-1NG, and VERITAS. The mission TanDEM-X, led by his institute, has generated a global, high-resolution digital elevation model of the Earth with unprecedented accuracy. He is the Initiator and the Principal Investigator (PI) for this mission. His professional interests and research areas encompass spaceborne radar end-to-end system design, microwave techniques and system concepts, signal processing, and remote sensing applications. He has authored or coauthored more than 450 publications in international conferences and journals, eight book chapters, and holds more than 40 international patent grants in the radar and antenna field. He has served as the President of the IEEE Geoscience and Remote Sensing (GRS) Society in 2010.

Dr. Moreira served as an Associate Editor of the IEEE GEOSCIENCE AND REMOTE SENSING LETTERS (GRS) from 2003 to 2007 and has been serving as an Associate Editor of the IEEE TRANSACTIONS ON GEOSCIENCE AND REMOTE SENSING (TGRS) since 2005. He was the General Co-Chair of International Geoscience and Remote Sensing Symposium (IGARSS) in 2012 and has been serving as the Chair of the Major Awards of the GRS Society since 2017. He was the Founder and the Chair of the Geoscience and Remote Sensing Society (GRSS) German Chapter from 2003 to 2008. He was a recipient of several international awards including the IEEE Aerospace and Electronic Systems Society (AESS) Nathanson Award in 1999, the IEEE Kiyo Tomiyasu Field Award in 2007, the IEEE W. R. G. Baker Award from the IEEE Board of Directors in 2012, and the IEEE GRSS Distinguished Achievement Award in 2014. He and his colleagues received the GRSS Transactions Prize Paper Awards in 1997, 2001, and 2007, and the GRSS Letters Prize Paper Award in 2015 and 2017. From 2012 to 2018, he has served as the Principal Investigator for the Helmholtz Alliance "Remote Sensing and Earth System Dynamics" in support of Tandem-L, a radar mission proposal for the global observation of dynamic processes on Earth's surface with unprecedented quality and resolution.